

Greenland Ice Sheet Ice Slab Expansion and Thickening

Nicolas Jullien¹, Andrew Jachnik Tedstone¹, Horst Machguth¹, Nanna B. Karlsson², and Veit Helm³

¹University of Fribourg

²GEUS

³Alfred Wegener Institute

March 28, 2023

Abstract

We use airborne accumulation radar data acquired over the Greenland Ice Sheet between 2002 and 2018 to identify changes in ice slab extent and thickness. We show that ice slabs several metres thick were already present at least as early as 2002. Between 2012 and 2018, they expanded 13,400-17,600 inland, or by 37-44%. Our results document that the extremely warm summer of 2012 produced near-surface ice layers at higher elevations, enabling ice slabs to develop in locations with only moderate melting in the following summers. With repeated flights over a transect in southwest Greenland, we show that ice slabs can thicken from above and on their undersides. Moderate melting primarily thickens ice slabs by top-down accretion, while large melting events can also trigger ice accretion below the slabs.

Greenland Ice Sheet Ice Slab Expansion and Thickening

N. Jullien¹, A. J. Tedstone¹, H. Machguth¹, N. B. Karlsson², V. Helm³

¹Department of Geosciences, University of Fribourg, Fribourg, Switzerland.

²Geological Survey of Denmark and Greenland, Copenhagen, Denmark.

³Alfred Wegener Institute, Helmholtz Centre for Polar and Marine Sciences, Bremerhaven, Germany.

Corresponding author: Nicolas Jullien (nicolas.jullien@unifr.ch)

Key Points:

- Ice slabs were already present in the early 2000s in southwest, central-west and north Greenland.
- Ice slabs expanded inland from 2002 to 2018 and thickened by top-down accretion and by accretion on their undersides.
- Near-surface ice layers support subsequent ice slab development.

15 Abstract

16 We use airborne accumulation radar data acquired over the Greenland Ice Sheet between 2002
17 and 2018 to identify changes in ice slab extent and thickness. We show that ice slabs several
18 metres thick were already present at least as early as 2002. Between 2012 and 2018, they
19 expanded 13,400-17,600 km² inland, or by 37-44%. Our results document that the extremely
20 warm summer of 2012 produced near-surface ice layers at higher elevations, enabling ice slabs
21 to develop in locations with only moderate melting in the following summers. With repeated
22 flights over a transect in southwest Greenland, we show that ice slabs can thicken from above
23 and on their undersides. Moderate melting primarily thickens ice slabs by top-down accretion,
24 while large melting events can also trigger ice accretion below the slabs.

25 Plain Language Summary

26 Above the equilibrium line elevation, seasonal snow is not entirely removed by summer melting.
27 As a result, firn - an interannual layer made of old snow and refrozen meltwater - builds up. Firn
28 holds the potential to buffer sea level rise by trapping liquid water within its pore space.
29 However, surface melting has increased in recent decades, making large quantities of water
30 available to percolate into the firn where it refreezes, eventually creating metres-thick ice slabs
31 that hinder future percolation. We mapped ice slabs in the subsurface firn (0-20m depth) by
32 using airborne radar surveys and show that they have expanded inland and thickened from 2002
33 to 2018. Once formed, ice slabs continue to thicken, even under moderate melt conditions.
34 Recent increases in the ice sheet's visible runoff area match well with the expansion of ice slabs,
35 so we conclude that ice slabs will be an important control on the future runoff area of the ice
36 sheet.

37 1 Introduction

38 In the 1990s, the mass balance of the Greenland Ice Sheet (GrIS) was close to equilibrium, but
39 has been negative for the last two decades (The IMBIE Team, 2020). Iceberg calving rates
40 increased (King et al., 2020; Rignot et al., 2008; The IMBIE Team, 2020) and the surface mass
41 balance (SMB) has decreased as a result of increasing melt and runoff (Enderlin et al., 2014;
42 Fettweis et al., 2017; The IMBIE Team, 2020; van den Broeke et al., 2016). Furthermore,
43 extremely warm summers such as in 2010, 2012, 2016 and 2019 (Mikkelsen et al., 2016;

44 Tedesco et al., 2011, 2013; Tedesco & Fettweis, 2020) triggered unprecedented surface melt
45 rates at high elevations (Hall et al., 2013; Nghiem et al., 2012) and exceptionally high volumes
46 of runoff (Mikkelsen et al., 2016; van Angelen et al., 2014).

47 Recent increases in surface melting have densified the subsurface firn (Machguth et al., 2016;
48 Mikkelsen et al., 2016; van Angelen et al., 2014). Firn is found above the equilibrium line and
49 consists of interannual snowpack, the density of which increases by compaction through burial
50 but also due to percolation and refreezing of surface meltwater (Braithwaite et al., 1994; Brown
51 et al., 2011; Pfeffer & Humphrey, 1998). Firn has the potential to trap and store meltwater within
52 its pore space, thereby buffering the GrIS contribution to sea level rise (Harper et al., 2012;
53 Pfeffer et al., 1991).

54 In the percolation zone, where surface melt rates are substantial but usually do not deplete the
55 seasonal snow completely, the fate of meltwater varies mainly with annual snowfall. Where
56 snowfall rates are high (~1000 +/- 400 mm w.e. per year), mostly in southeast and south
57 Greenland, liquid water percolates to a depth where it forms perennial firn aquifers (Forster et
58 al., 2014; Miège et al., 2016; Miller et al., 2022). Conversely, in regions where accumulation
59 rates are lower and which have recently experienced significant melting, ice slabs several metres
60 thick can form – mostly along the west, north and northeast of the GrIS (MacFerrin et al., 2019;
61 Miller et al., 2022). In these regions, increased meltwater percolation during several successive
62 summers fused centimeters-scale ice lenses into increasingly contiguous ice layers tens of
63 centimeters thick and eventually metres-thick slabs, thereby decreasing the firn's permeability
64 (de la Peña et al., 2015; Vandecrux et al., 2019). Ice slabs form an aquitard, preventing most
65 subsequent meltwater from reaching the relict pore space below (MacFerrin et al., 2019;
66 Machguth et al., 2016).

67 Ice slabs favour the development of surface streams in the high percolation zone (Machguth et
68 al., 2016; Mikkelsen et al., 2016; Tedstone & Machguth, 2022). The area of the ice sheet drained
69 by surface rivers increased by 29% between 1985 and 2020, corresponding strongly with the
70 locations of ice slabs mapped previously and suggesting that 5-10% of recent ice-sheet-wide
71 mass losses originated from these newly densified parts of the accumulation zone (Tedstone &
72 Machguth, 2022). This underlines that it is essential to understand firn densification and ice slab

73 development for inclusion in ice sheet mass balance models that are used for projections of
74 future ice sheet runoff (de la Peña et al., 2015). Despite their emerging importance to future
75 runoff magnitude, ice slabs have only been mapped over a short time period: with accumulation
76 radar from 2010 to 2014 (MacFerrin et al., 2019), and through a proxy approach with satellite
77 microwave radiometry from 2015 to 2019 (Miller et al., 2022). Here we investigate changes in
78 the extent and thickness of ice slabs using airborne radar observations acquired during spring-
79 time campaigns between 2002 and 2018.

80 **2 Data and Methods**

81 To map ice layer and slab locations in 2002-03 we used data collected by 600-900 MHz
82 accumulation radar (Kanagaratnam et al., 2004; Lewis, 2010). To examine changing ice content
83 during 2010-18, we used the 550-900 MHz accumulation radar (Carl et al., 2011; CReSIS, 2021;
84 Rodriguez-Morales et al., 2010) ; the 2010-14 data that we processed are identical to those used
85 by MacFerrin et al. (2019).

86 Data acquired during 2002-03 were detrended in the logarithmic domain by the provider, so they
87 have virtually no radiometric information (J. Paden, personal communication 2020). This means
88 they are only useful for layer tracking. Nevertheless, the radiometric variability of the signal is
89 large enough to enable manual ice identification (Text S1). For radargrams acquired between
90 2010 and 2018, we developed a semi-automated approach based on MacFerrin et al. (2019) (Text
91 S2). In brief, to prepare the radargrams we picked the ice sheet surface, corrected for the roll of
92 the aircraft, removed the impact of varying atmospheric conditions by subtracting the average
93 surface signal strength, and applied a correction for depth attenuation.

94 We aimed to detect changes sub-surface ice thickness through time. MacFerrin et al. (2019) used
95 a normalised threshold to detect ice content, but we found that this yielded strong differences
96 between co-located radargrams over successive years (Text S2). Instead, we examined a range of
97 radar signal strengths extracted from a “reference” radargram as thresholds to discriminate
98 between porous firn and ice content in the uppermost 20 m. To determine the appropriate range
99 of radar signal strengths, we first manually digitised ice content in the reference radargram based
100 on comparison with in-situ ground penetrating radar measurements and firn cores acquired by
101 MacFerrin et al. (2019) (Fig. S3). Next, we used our reference radargram to determine the signal

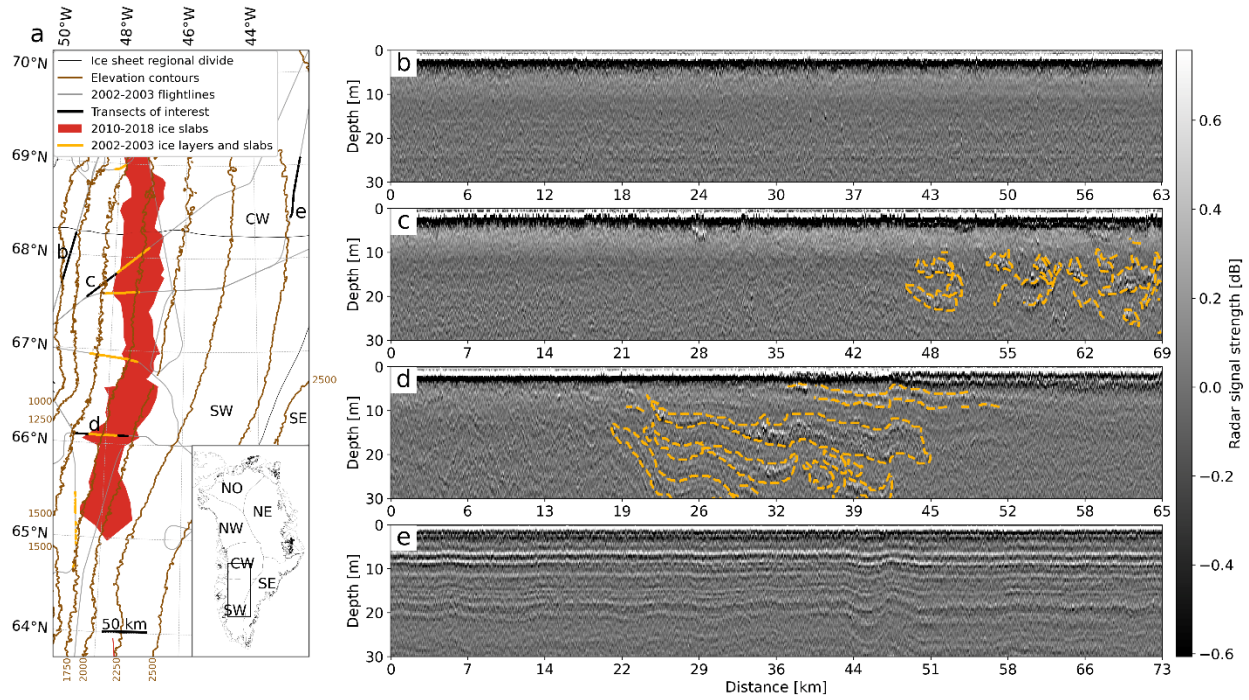
102 return strength given by (a) ice content versus (b) porous firn. The signal distributions of ice
103 content and porous firn partially overlap (Fig. S4). Following a sensitivity analysis (Text S2), we
104 chose lower and upper signal strength thresholds which correspond to the minimum and
105 maximum likely ice content, respectively. The producer's accuracy (overall accuracy) in
106 detecting ice content is 53% (86%) at the lower threshold and 73% (88%) at the higher threshold
107 (Tables S1, S2). For each radargram we also estimated the likelihood of ice content presence
108 between the lower and upper thresholds when ice is first detected. Thus, 100% ice likelihood
109 corresponds to detection at the lower threshold, while 50% corresponds to detection mid-way
110 between the lower and upper thresholds. Finally, following MacFerrin et al., (2019), we identify
111 ice slabs where radar-detected ice content is at least 1 m thick, and consider them to have a
112 maximum accumulation radar-detected thickness of 16 m. We use the term 'ice layers' to refer to
113 ice content less than ~1 m thick.

114 As a proxy for surface melting, we calculated Positive Degree Hour sum using a similar
115 approach to degree-day modelling (Hock, 2003), using in-situ 2 m air temperature measurements
116 from 2009 to 2017 at the automatic weather station KAN_U (Fausto et al., 2021). We summed
117 every positive 1-hour average temperature (i.e. above 0°C) for each year.

118 **3 Results**

119 3.1 Ice slab expansion from 2002 to 2018

120 Ice layers and slabs were present in 2002-03 (Fig. 1, 2a), up to several meters thick in SW
121 Greenland (Fig. 1a,c-d). Although the observations are relatively sparse (Fig. S7a), they were
122 also identified in the CW, in the vicinity of Sermeq Kujalleq's (Jakobshavn Isbrae) high
123 percolation zone. Ice layers and slabs were identified in the NO but not in the NW nor the NE,
124 although spatial coverage was limited in the latter regions.

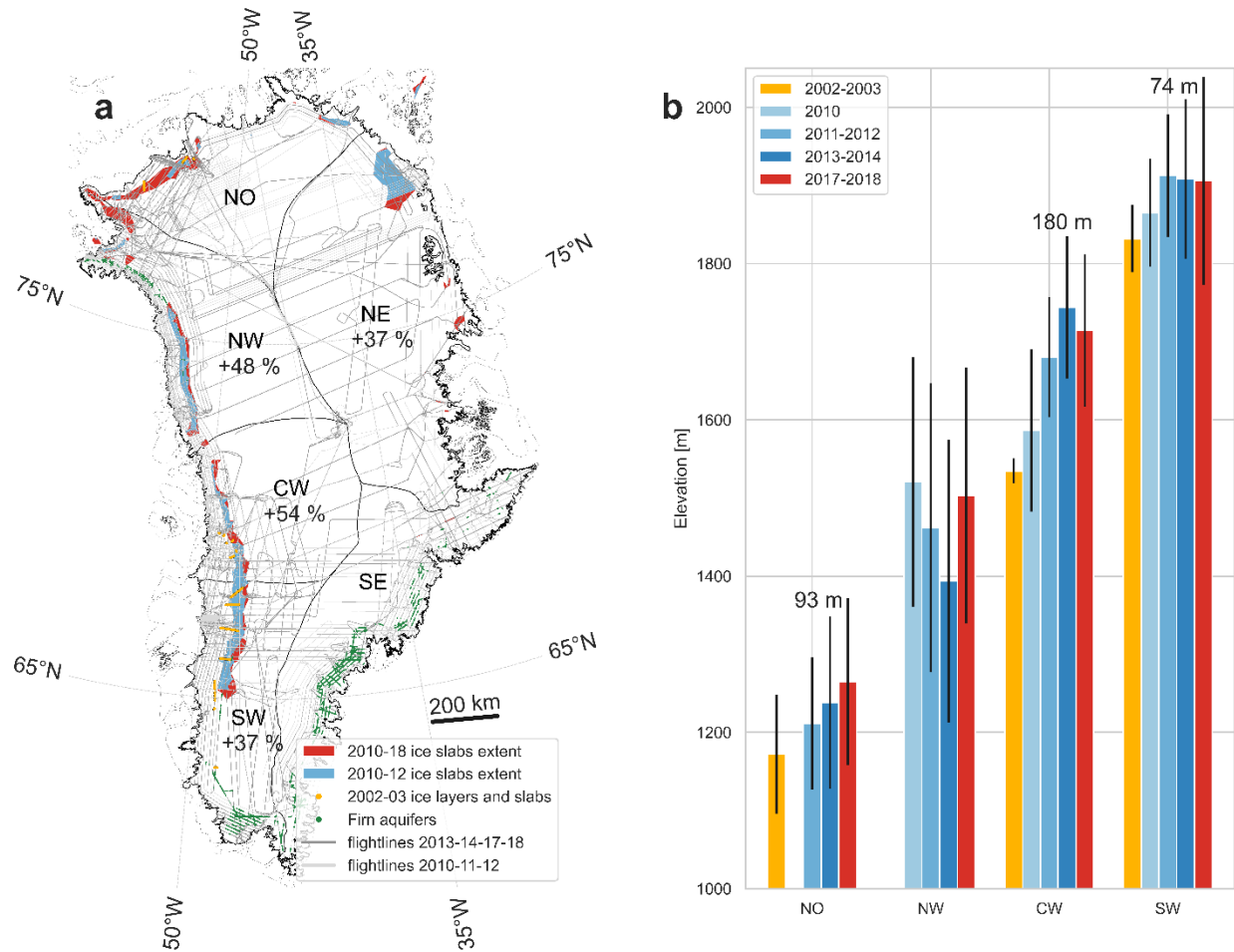


125

126 **Figure 1.** Ice layers and slabs in central and southwest Greenland in 2002-2003. (a) Regional
 127 zoom of radargram locations. Radargrams with ice layers/slabs identification overlaid (orange
 128 dashed lines) acquired from the (b) ablation zone (c-d) percolation zone and (e) dry snow zone.

129

130



131

132 **Figure 2.** Ice slab extent from 2002 to 2018. (a) Ice layers and slabs in 2002-03 (orange), ice
 133 slab extent in 2010-12 (blue) and 2010-18 (red), firn aquifers in 2010-2014 (Miège et al., 2016)
 134 (green). Ice slab extents are derived from multiple flight lines (Fig. S8). Flight lines used for
 135 identification of 2010-2018 ice slabs (light grey: 2010-12, dark grey: 2013-18). Percentages
 136 indicate the upglacier expansion of ice slab extent in 2017-2018 with respect to 2010-12. (b)
 137 Maximum ice slab elevation (coloured bars) +/- 1 standard deviation (black bars) in each region.
 138 Numbers indicate the change in maximum ice slab elevation between 2002-03 and 2017-18.
 139 Elevations are above WGS84 ellipsoid. Maximum elevation changes in the NE, are omitted, as
 140 well as extent change in the NO and north of the NW as there was insufficient overlap in flight
 141 lines between the different periods (Fig. S7a-e).

142

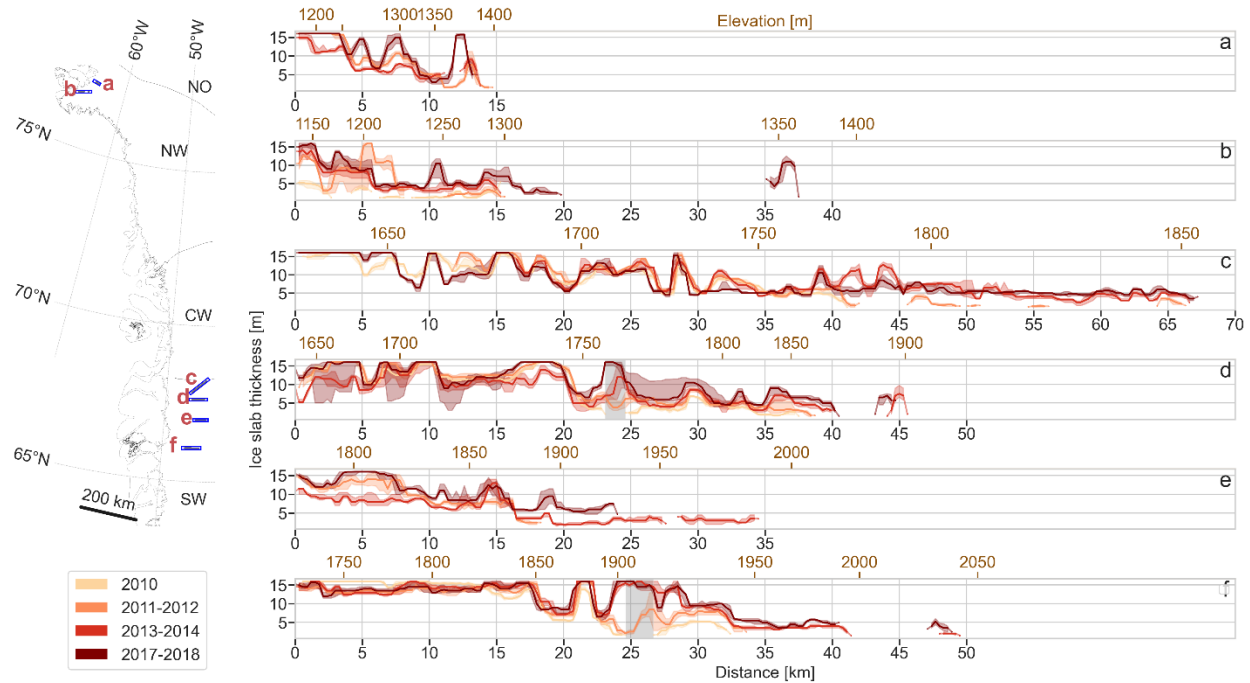
143 Considering the extents of our slab retrievals (Figs. 2a, S8), ice slabs occupied over 60,400-
144 73,500 km^2 (low-high bounds) in 2018, consistent with 2015-2019 ice slabs retrievals extending
145 over 76,000 km^2 using satellite microwave radiometry by Miller et al., (2022). Except in the
146 southern part of SW Greenland, we did not identify any entirely new ice slabs in either 2002-03
147 or 2017-18 compared to the 2010-14 mapping performed by MacFerrin et al., (2019) (Fig. S8).

148 We examined inland expansion between 2010-12 and 2017-18 (Fig. 2a). We use 2010-12
149 because there is good spatial coverage in 2011-12 supported by complementary coverage in 2010
150 (Fig. S7b-e). We estimate that the ice slab area increased from 2010-12 to 2017-18 by 37% in the
151 NE and the SW, 48% in the NW, and 54% in the CW. We also calculated the maximum ice slab
152 elevation in each period by picking the maximum elevation in 10 km-wide boxes, then
153 calculating the median value in each region. This showed that the increase in area was driven by
154 ice slab expansion to higher elevations throughout the west coast (Figs. 2b, S8), in agreement
155 with the upslope expansion of ice slabs identified by Miller et al., (2022).

156 3.2 Ice slab thickening

157 The accumulation radar used between 2010 and 2018 has a vertical resolution of 65 cm in snow
158 and firn (Rodriguez-Morales et al., 2014), enabling the examination of changes in ice slab
159 thickness along repeated radar survey lines. We focus on six transects which had repeated radar
160 surveys within tens to hundreds of metres of each other (Fig. 3) and differentiate between three
161 stages of ice slab change between 2010 and 2018: (i) initiation (i.e. appearance of a ~meter-thick
162 slab), (ii) development (i.e. significant thickening of existing ice slab) and (iii) well-developed
163 (i.e. already at least 10 m thick) (Text S3, Fig. S5). Ice content increased between 2010 and 2018
164 along all the transects. While there were no major thickness changes where well-developed ice
165 slabs were already present in 2010 (e.g. Fig. 3f from 0 to 23 km), we observed development of
166 thinner ice slabs. On transect A, ice content at 11-13 km increased by 13.5 m between 2011-12
167 and 2017-18. On transect B, the slab at 8-15 km thickened from less than 2 m in 2010 to roughly
168 5 m by 2017-18.

169



170

171 **Figure 3.** Ice slab thickness over time. Ice thickness derived from our upper ice content detection
 172 threshold (quantile 0.79). For each transect, the data were aggregated from the start of the
 173 transect into 300 m bins, smoothed with a 900 m rolling median. Median in bold, interquartile
 174 range denoted by shading.

175 Previously discontinuous ice slabs merged laterally over time (Fig. 3b-d,f). On transect C, a 5 to
 176 10 m-thick ice slab developed above the 2010 upper limit (at 41 km) by 2013-14, fusing several
 177 previously thinner and isolated areas of ice slab. Consequently, the upper limit of ice slabs
 178 expanded inland by 26 km from 2010 to 2017. On transect D (Fig. 3d), the ice-free section in
 179 between 23-24.5 km (grey shading) saw initial ice slab generation during summer 2010. This
 180 area developed to 16 m by 2018, filling the gap between two previously unconnected slabs and
 181 expanding the continuous ice slab by 17.4 km. Similar behaviour is apparent in transect F (Fig.
 182 3f grey shading).

183 To examine ice slab initiation and thickening in more detail, we examined radargrams along a
 184 transect with good repeat radar coverage near to the KAN_U weather station at which
 185 meteorological measurements have been made continuously since 2009 (Fig. 4). No radar data
 186 were acquired in this area during 2002-03, but radargrams acquired in the nearby area during

187 2010 and 2011 show sub-surface decimeters to meters-thick ice content (Fig. S9a-b). 2014 and
188 2017 radargrams are offset by several hundreds of meters from 2012, 2013 and 2018 radargrams
189 (900 m at 13.8 km, 1700 m at 40 km, Fig. 4a). The ice content can vary significantly between
190 non-perfectly overlapping transects. For example, the ice content between 13.8 and 15.6 km is
191 ~59% less in the 2014 retrieval compared to 2013 (Fig. 4b-c). Nonetheless, we still detected
192 overall thickening through time (Figs. 4d, S9h). Between 2012 and 2018, the ice thickened
193 between 0 and 13.8 km (+9%), increased substantially between 13.8 and 17.7 km (+43%), and a
194 new ice slab developed from 18.5 km.

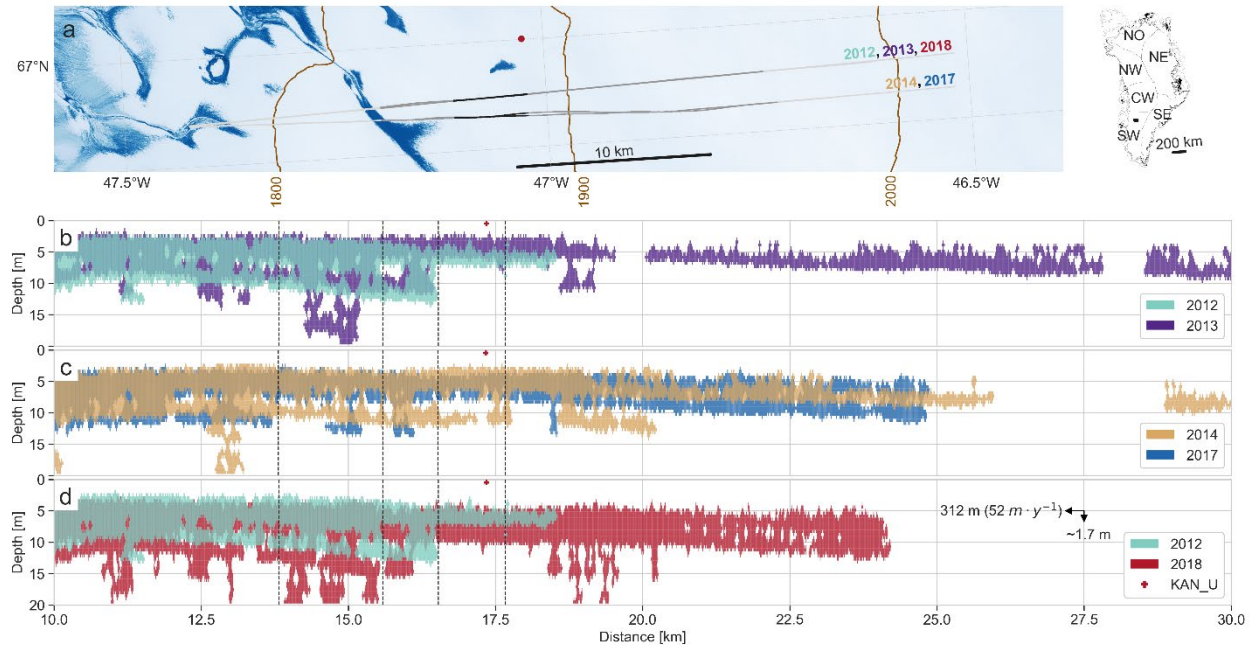
195 To relate the changes in ice thickness to the potential for meltwater percolation and refreezing,
196 we used total annual Positive Degree Hours (PDH) as a first-order estimate of summer melting
197 (Fig. S6). Following the extreme melt-year of 2012 with 1273 °C PDH, ice content between 13.8
198 and 17.7 km increased by 4,576 m² (19 %) from spring 2012 to spring 2013. From summer 2013
199 to 2017 there were 2233 °C PDH – 175% of 2012 – yet ice content increased by only 5,738 m²
200 between spring 2013 and spring 2018, equivalent to 25 % more ice content formation than 2012
201 alone.

202 We observed that ice slabs can thicken by ice accretion (i) on top of existing ice content versus
203 (ii) beneath. Considering top-down accretion, between 16.5 to 17.7 km there was 2.9 m
204 thickening from above between 2012 and 2018 (Fig. 4d); the bottom of the slab deepened by 3 m
205 with respect to the surface due to gradual burial (Text S4). Directly beneath KAN_U, 0.8 m ice
206 was added to the top of the ice slab due to high PDH in summer 2012 (Fig. 4b), and 0.6 m during
207 summer 2013 (Figs. 4b-c, S9h), even though the 2013 PDH was only 30% of the 2012 PDH (Fig.
208 S6). The subsequent 2.5 m of top-down thickening between 2014 and 2018 occurred during only
209 moderate melting in 2014 and 2016 and limited melting in 2015 and 2017 (Figs. 4c-d, S6, S9e-
210 h). There is further evidence of accretion on top of existing ice slabs in transects C-F (Fig. S10).

211 Between 13.8 and 15.6 km there was ~4 m of thickening predominantly below the slab between
212 2012 and 2018 (Fig. 4b,d). This was generated by ~1.5 m of accretion predominantly below the
213 existing ice slab due to summer 2012 (Fig. 4b), and a further ~2.5 m of accretion during 2014-
214 2017 split between thickening from above and below (Figs. 4b,d, S9d,g). We also observed
215 localized accretion below existing ice slabs in transects A, B and E (Fig. S10).

216 Ice slab expansion to higher elevations predominantly occurred through accretion on top of
 217 existing near-surface ice layers. At 2012's upper ice slab boundary (18.5 km), a ~1 m layer grew
 218 by spring 2013, subsequently thickening to 6 m by 2018 and yielding 5.7 km of inland slab
 219 expansion (Fig. 4d). Conversely, from ~25 km onwards the near-surface ice layer identified in
 220 spring 2013 (Fig. 4b) was buried by subsequent accumulation (Fig. 4d).

221



222

223 **Figure 4.** Ice thickness change through time along a transect close to KAN_U. (a) Near-infrared
 224 (band 8) Sentinel-2 image acquired on August 23rd, 2021, complete radargram extent (light
 225 grey), radargram extent (dark grey) shown in panels b-d, ~4km transect of interest (black),
 226 location of KAN_U (red dot). (b-d) Maximum likely ice content between different repeat
 227 radargrams. The dashed vertical lines delineate specific areas discussed in the text. In panel d,
 228 the vertical arrow illustrates burial from 2013 to 2017 due to firn replenishment; the horizontal
 229 arrow illustrates the lateral movement of the ice from 2012 to 2018 (Text S4).

230 4 Discussion

231 4.1 Mechanisms of ice slab formation and thickening

232 We identify three principal mechanisms of ice slab formation and thickening. (i) Meltwater
233 percolation and refreezing generates initial ice layers in porous firn. Then, accretion of ice by
234 meltwater refreezing proceeds (ii) on top of, and/or (iii) beneath pre-existing ice layers.

235 In the data presented in Fig. 4, mechanism (i) was responsible for the initial generation of a 3 m-
236 thick near-surface contiguous ice slab by the fusing of pre-existing discontinuous ice layers in
237 porous firn from 18.5 km onwards during summer 2012. Culberg et al. (2021) and de la Peña et
238 al. (2015) similarly showed that the initiation of near-surface ice layers can occur within a single
239 extremely warm summer.

240 Radar observations can differentiate between subsequent thickening by accretion (ii) on top of,
241 and (iii) below existing ice content. We interpret that unexceptional but sustained melting
242 conditions such as in 2014 or 2016 predominantly cause thickening by accretion on top of pre-
243 existing ice slabs (Figs. 4c, S6, S9c-g). Machguth et al., (2016) also evidenced top-down ice
244 accretion due to the 2013 and 2014 moderate melt summers by comparing 2015 and 2013 cores.
245 Hence, once ice slabs form, they thicken even in moderate melt years.

246 Accretion below existing ice slabs (Fig. 4b,d) was primarily associated with the large PDH sum
247 during summer 2012 (Fig. S6). We propose that abundant meltwater - which may have
248 originated from higher elevations (Clerx et al., 2022) - was able to exploit local areas of higher
249 permeability. Previous observations show that deep percolation (> 10 m) can occur in firn
250 without homogeneous wetting front advance (Humphrey et al., 2012; Machguth et al., 2016;
251 Samimi et al., 2020). However, these processes are less likely to occur through several meters
252 thick ice slabs. In northwest Greenland, Culberg et al., (2022) found that meltwater associated
253 with visible runoff features probably exploits fractures to penetrate through the ice slab and
254 refreeze underneath. We find multiple lines of evidence which support this process further south.
255 First, crevasses have been observed at high elevations in the percolation zone of central-west
256 Greenland (Colgan et al., 2016), providing paths for meltwater to flow vertically. Second, the
257 accretion of ice beneath ice slabs observed downstream of KAN_U (Fig. 4) is associated with
258 meltwater ponding in a slush field (Fig. S11). Third, sudden firn warming at 5 m depth at

259 KAN_U in September 2012 strongly supports abrupt meltwater penetration through a 3 m thick
260 ice slab, followed by gradual cooling through winter indicative of refreezing (Machguth et al.,
261 (2016) Figs. S4 and S5a). Finally, firn cores acquired in 2012 and 2013 show ice accretion at a
262 depth of 5 m in-between existing ice slabs (Machguth et al., (2016) Fig. S4c).

263 4.2 Changes in sub-surface firn and implications

264 Immediately above the current ice slab extent in SW Greenland, the firn is primed for further ice
265 slab development. Indeed, cores from Site J (2040 m asl) acquired in 1989 and 2017 clearly
266 show the merging of ice lenses into several ~1 m thick layers in the uppermost 12 m
267 (Rennermalm et al., 2021), and cores acquired at Dye-2 (2,120 m asl) in 1998 and 2013 tell a
268 similar story (Machguth et al., 2016). The increase in firn density and ice content is consistent
269 with recent warmer surface conditions (de la Peña et al., 2015).

270 Surface melting is projected to increase in the percolation zone (Fettweis et al., 2013; Franco et
271 al., 2013), and extreme summer melting events such as 2010 and 2012 are expected to become
272 more frequent (Bevis et al., 2019). Yet, radargrams indicate that the fate of the near-surface ice
273 layer generated in summer 2012 varied by elevation.

274 Towards the lower elevations of the ice layer that was mostly generated due to summer 2012
275 (from 18.5 km onwards), additional ice accreted, forming ice slabs by 2017-18 (Fig. 4).
276 Conversely, at higher elevations where melt was infrequent between 2013 and 2017 (Fig. S6),
277 the near-surface layer generated in 2012 was progressively buried to moderate depths, reducing
278 the likelihood that it will support ice slab growth in the future. The upper limit of the summer
279 2012 ice layer (Fig. S9d) is located 260 m away from the location of Core 3 (Rennermalm et al.,
280 2021). The later layer probably corresponds to the numerous ice layers found in the uppermost 9
281 m of Core 3 in 2013. By 2018, these ice layers had been buried and could no longer be identified
282 by radar (Fig. S9e-g), in agreement with ~3.5 m of firn replenishment identified by the redrilling
283 of Core 3 in 2019. This is consistent with Culberg et al. (2021), who showed that the 2012 near-
284 surface melt layer above 2600 m asl in central Greenland was initially located at 1 m deep, and
285 was still present in 2017 but had been buried to a depth of 5 m. Thus, the ability of near-surface
286 ice layers to support subsequent ice slab development is likely to depend on whether strong
287 melting occurs during several successive summers.

288 Considering recent sub-surface changes between 2013 and 2017, cores at KAN_U (Fig. 6a in
289 Rennermalm et al. (2021)) show that the top of the ice slab was at roughly the same depth in
290 2017 as 2013. However, the 2015 and 2016 cores showed some evidence of firn replenishment.
291 We suggest that this replenishment subsequently melted during summer 2016 (Fig. S6) and
292 refroze on top of the slab. Thus, the effect of isolated years of firn replenishment, which
293 temporarily bury an ice slab, can be easily erased by relatively moderate melting.

294 **5 Conclusions**

295 We interpreted accumulation radar data to show that ice slabs already existed in 2002-03 in SW,
296 CW and NO Greenland, which are most likely a result of increasing surface melting from the
297 mid-1990s onwards (van As et al., 2016). On an ice-sheet-wide basis we showed that ice slabs
298 expanded inland from 2012 to 2018 by 13,400-17,600 km², or 37-44%.

299 We identified two mechanisms by which ice slabs thicken: wide-spread ice accretion on top of
300 pre-existing ice slabs, and more localised ice accretion beneath pre-existing ice slabs. We
301 suggest that deep percolation through ice slabs takes place beneath ponded surface meltwater
302 features and exploits local fractures in otherwise near-impermeable ice slabs. Accretion below
303 pre-existing ice slabs is therefore more likely during extreme melt seasons, while more moderate
304 melt seasons predominantly result in top-down thickening.

305 Extremely warm summers such as 2012 can produce enough meltwater at higher elevations to
306 generate a near-surface ice layer on the order of at least a meter thick, forming the basis for
307 subsequent ice slab expansion via top-down ice accretion. Once formed, ice slabs continue to
308 thicken, even under moderate melting conditions.

309 We suggest that future increases in melting at higher elevations will trigger further ice slab
310 development, increasing the ice slab area non-linearly with elevation because of the non-linearity
311 of the hypsometry of the ice sheet (Bauer, 1955). The recent expansion of the visible runoff area
312 of the Greenland Ice Sheet (Tedstone & Machguth, 2022) is strongly linked with the expansion
313 of ice slabs (Fig. S12), so future increases in ice slab area are likely to further increase the area
314 which contributes runoff to the oceans.

315 **Acknowledgments**

316 This work was funded under the European Research Council award 818994 – CASSANDRA.
317 We acknowledge the use of data and data products from CReSIS generated with support from
318 the University of Kansas, NASA Operation IceBridge grant NNX16AH54G, NASA grant
319 NNX10AT68G, NSF grants ACI-1443054, OPP-1739003, and IIS-1838230, ANT-0424589,
320 Lilly Endowment Incorporated, and the Indiana METACyt Initiative. We thank P. Bednawrek
321 (University of Fribourg) for computational support.

322 **Open Research**

323 2002-2003 and 2010-2018 accumulation radar data (CReSIS, 2021) are available on the CReSIS
324 data repository (<https://data.cresis.ku.edu/data/accum/>). We used the ArcticDEM digital
325 elevation model at 100m resolution, which provides elevation above the WGS84 ellipsoid
326 (<https://www.pgc.umn.edu/data/arcticdem/>). The regional divisions of the GrIS are based on the
327 Greenland Ice Sheet drainage basins from Rignot & Mouginot (2012). Air temperatures at the
328 automatic weather station KAN_U station can be downloaded from
329 <https://doi.org/10.22008/promice/data/aws>. Sentinel 2 satellite images can be downloaded at
330 <https://scihub.copernicus.eu/dhus/#/home>. The scripts used to perform the analysis for this study
331 can be found at https://github.com/jullienn/changing_Greenland_iceslabs. Our ice slab dataset is
332 available at <https://doi.org/10.5281/zenodo.7505426>.

333 **Author contributions**

334 NJ, AT and HM designed the study. NK contributed to interpretation of the 2002-03 radargrams.
335 NJ developed the methodology for ice identification in 2010-18 data, with contributions from
336 VH, HM and AT. NJ carried out data processing, data analysis and interpretation. NJ and AT
337 wrote the manuscript based on comments from all co-authors.

338 **References**

339 Bauer, A. (1955). The Balance of the Greenland Ice Sheet. *Journal of Glaciology*, 2(17), 456–462. Cambridge Core.
340 <https://doi.org/10.3189/002214355793702271>
341 Bevis, M., Harig, C., Khan, S. A., Brown, A., Simons, F. J., Willis, M., Fettweis, X., van den Broeke, M. R.,
342 Madsen, F. B., Kendrick, E., Caccamise, D. J., van Dam, T., Knudsen, P., & Nylén, T. (2019). Accelerating changes
343 in ice mass within Greenland, and the ice sheet's sensitivity to atmospheric forcing. *Proceedings of the National*
344 *Academy of Sciences*, 116(6), 1934–1939. <https://doi.org/10.1073/pnas.1806562116>

- 345 Braithwaite, R. J., Laternser, M., & Pfeffer, W. T. (1994). Variations of near-surface firn density in the lower
346 accumulation area of the Greenland ice sheet, Pâkitsoq, West Greenland. *Journal of Glaciology*, 40(136), 477–485.
347 Cambridge Core. <https://doi.org/10.3189/S002214300001234X>
- 348 Brown, J., Harper, J., Pfeffer, W. T., Humphrey, N., & Bradford, J. (2011). High-resolution study of layering within
349 the percolation and soaked facies of the Greenland ice sheet. *Annals of Glaciology*, 52(59), 35–42.
350 <https://doi.org/10.3189/172756411799096286>
- 351 Carl, L., Lewis, C., Gogineni, P., Rodriguez, F., Paden, J., & Li, J. (2011). *IceBridge Accumulation Radar LIB*
352 *Geolocated Radar Echo Strength Profiles, 2010, 2011, 2012, 2013, 2014, 2017, 2018 [Dataset]*. Boulder, Colorado
353 USA: National Snow and Ice Data Center. Digital media. <https://data.cresis.ku.edu/data/accum/>.
- 354 Clerx, N., Machguth, H., Tedstone, A., Jullien, N., Wever, N., Weingartner, R., & Roessler, O. (2022). *In situ*
355 *measurements of meltwater flow through snow and firn in the accumulation zone of the SW Greenland Ice Sheet*
356 [Preprint]. Ice sheets/Glacier Hydrology. <https://doi.org/10.5194/egusphere-2022-71>
- 357 Colgan, W., Rajaram, H., Abdalati, W., McCutchan, C., Mottram, R., Moussavi, M. S., & Grigsby, S. (2016).
358 Glacier crevasses: Observations, models, and mass balance implications: Glacier Crevasses. *Reviews of Geophysics*,
359 54(1), 119–161. <https://doi.org/10.1002/2015RG000504>
- 360 CReSIS. (2021). *Accumulation radar Data, 2002, 2003, 2010, 2011, 2012, 2013, 2014, 2017, 2018 [Dataset]*
361 *Lawrence, Kansas, USA. Digital Media*. <http://data.cresis.ku.edu/>
- 362 Culberg, R., Chu, W., & Schroeder, D. M. (2022). Shallow Fracture Buffers High Elevation Runoff in Northwest
363 Greenland. *Geophysical Research Letters*, 49(23). <https://doi.org/10.1029/2022GL101151>
- 364 Culberg, R., Schroeder, D. M., & Chu, W. (2021). Extreme melt season ice layers reduce firn permeability across
365 Greenland. *Nature Communications*, 12(1), 2336. <https://doi.org/10.1038/s41467-021-22656-5>
- 366 de la Peña, S., Howat, I. M., Nienow, P. W., van den Broeke, M. R., Mosley-Thompson, E., Price, S. F., Mair, D.,
367 Noël, B., & Sole, A. J. (2015). Changes in the firn structure of the western Greenland Ice Sheet caused by recent
368 warming. *The Cryosphere*, 9(3), 1203–1211. <https://doi.org/10.5194/tc-9-1203-2015>
- 369 Enderlin, E. M., Howat, I. M., Jeong, S., Noh, M.-J., van Angelen, J. H., & van den Broeke, M. R. (2014). An
370 improved mass budget for the Greenland ice sheet. *Geophysical Research Letters*, 41(3), 866–872.
371 <https://doi.org/10.1002/2013GL059010>
- 372 Fausto, R. S., van As, D., Mankoff, K. D., Vandecrux, B., Citterio, M., Ahlstrøm, A. P., Andersen, S. B., Colgan,
373 W., Karlsson, N. B., Kjeldsen, K. K., Korsgaard, N. J., Larsen, S. H., Nielsen, S., Pedersen, A. Ø., Shields, C. L.,
374 Solgaard, A. M., & Box, J. E. (2021). *Programme for Monitoring of the Greenland Ice Sheet (PROMICE) automatic*
375 *weather station data*. 27.
- 376 Fettweis, X., Box, J. E., Agosta, C., Amory, C., Kittel, C., Lang, C., van As, D., Machguth, H., & Gallée, H. (2017).
377 Reconstructions of the 1900–2015 Greenland ice sheet surface mass balance using the regional climate MAR model.
378 *The Cryosphere*, 19.
- 379 Fettweis, X., Franco, B., Tedesco, M., van Angelen, J. H., & Lenaerts, J. T. M. (2013). Estimating the Greenland ice
380 sheet surface mass balance contribution to future sea level rise using the regional atmospheric climate model MAR.
381 *The Cryosphere*, 21.
- 382 Fettweis, X., Hofer, S., Krebs-Kanzow, U., Amory, C., Aoki, T., Berends, C. J., Born, A., Box, J. E., Delhasse, A.,
383 Fujita, K., Gierz, P., Goelzer, H., Hanna, E., Hashimoto, A., Huybrechts, P., Kapsch, M.-L., King, M. D., Kittel, C.,
384 Lang, C., ... Tedesco, M. (2020). GrSMBMIP: intercomparison of the modelled 1980–2012 surface mass balance
385 over the Greenland Ice Sheet. *The Cryosphere*, 24.
- 386 Forster, R. R., Box, J. E., van den Broeke, M. R., Miège, C., Burgess, E. W., van Angelen, J. H., Lenaerts, J. T. M.,
387 Koenig, L. S., Paden, J., Lewis, C., Gogineni, S. P., Leuschen, C., & McConnell, J. R. (2014). Extensive liquid
388 meltwater storage in firn within the Greenland ice sheet. *Nature Geoscience*, 7(2), 95–98.
389 <https://doi.org/10.1038/ngeo2043>
- 390 Franco, B., Fettweis, X., & Erpicum, M. (2013). Future projections of the Greenland ice sheet energy balance
391 driving the surface melt. *The Cryosphere*, 7(1), 1–18. <https://doi.org/10.5194/tc-7-1-2013>
- 392 Hall, D. K., Comiso, J. C., DiGirolamo, N. E., Shuman, C. A., Box, J. E., & Koenig, L. S. (2013). Variability in the
393 surface temperature and melt extent of the Greenland ice sheet from MODIS: TEMPERATURE AND MELT OF
394 GREENLAND ICE. *Geophysical Research Letters*, 40(10), 2114–2120. <https://doi.org/10.1002/grl.50240>
- 395 Harper, J., Humphrey, N., Pfeffer, W. T., Brown, J., & Fettweis, X. (2012). Greenland ice-sheet contribution to sea-
396 level rise buffered by meltwater storage in firn. *Nature*, 491(7423), 240–243. <https://doi.org/10.1038/nature11566>
- 397 Hock, R. (2003). Temperature index melt modelling in mountain areas. *Journal of Hydrology*, 282(1–4), 104–115.
398 [https://doi.org/10.1016/S0022-1694\(03\)00257-9](https://doi.org/10.1016/S0022-1694(03)00257-9)

- 399 Humphrey, N. F., Harper, J. T., & Pfeffer, W. T. (2012). Thermal tracking of meltwater retention in Greenland's
400 accumulation area: THERMAL TRACKING OF MELTWATER RETENTION. *Journal of Geophysical Research:*
401 *Earth Surface*, 117(F1), n/a-n/a. <https://doi.org/10.1029/2011JF002083>
- 402 Kanagaratnam, P., Gogineni, S. P., Ramasami, V., & Braaten, D. (2004). A Wideband Radar for High-Resolution
403 Mapping of Near-Surface Internal Layers in Glacial Ice. *IEEE Transactions on Geoscience and Remote Sensing*,
404 42(3), 483–490. <https://doi.org/10.1109/TGRS.2004.823451>
- 405 Karlsson, N. B., Colgan, W. T., Binder, D., Machguth, H., Abermann, J., Hansen, K., & Pedersen, A. Ø. (2019). Ice-
406 penetrating radar survey of the subsurface debris field at Camp Century, Greenland. *Cold Regions Science and*
407 *Technology*, 165, 102788. <https://doi.org/10.1016/j.coldregions.2019.102788>
- 408 King, M. D., Howat, I. M., Candela, S. G., Noh, M. J., Jeong, S., Noël, B. P. Y., van den Broeke, M. R., Wouters,
409 B., & Negrete, A. (2020). Dynamic ice loss from the Greenland Ice Sheet driven by sustained glacier retreat.
410 *Communications Earth & Environment*, 1(1), 1. <https://doi.org/10.1038/s43247-020-0001-2>
- 411 Lewis, C. (2010). *Airborne UHF Radar for Fine Resolution Mapping of Near-Surface Accumulation Layers in*
412 *Greenland and West Antarctica*, (Master's thesis) [University of Kansas]. Retrieved from KU Scholar Works data
413 repository (<http://hdl.handle.net/1808/7008>)
- 414 MacFerrin, M., Machguth, H., As, D. van, Charalampidis, C., Stevens, C. M., Heilig, A., Vandecrux, B., Langen, P.
415 L., Mottram, R., Fettweis, X., Broeke, M. R. van den, Pfeffer, W. T., Moussavi, M. S., & Abdalati, W. (2019).
416 Rapid expansion of Greenland's low-permeability ice slabs. *Nature*, 573(7774), 403–407.
417 <https://doi.org/10.1038/s41586-019-1550-3>
- 418 Machguth, H., MacFerrin, M., van As, D., Box, J. E., Charalampidis, C., Colgan, W., Fausto, R. S., Meijer, H. A. J.,
419 Mosley-Thompson, E., & van de Wal, R. S. W. (2016). Greenland meltwater storage in firn limited by near-surface
420 ice formation. *Nature Climate Change*, 6(4), 390–393. <https://doi.org/10.1038/nclimate2899>
- 421 Miège, C., Forster, R. R., Brucker, L., Koenig, L. S., Solomon, D. K., Paden, J. D., Box, J. E., Burgess, E. W.,
422 Miller, J. Z., McNerney, L., Brautigam, N., Fausto, R. S., & Gogineni, S. (2016). Spatial extent and temporal
423 variability of Greenland firn aquifers detected by ground and airborne radars. *Journal of Geophysical Research:*
424 *Earth Surface*, 121(12), 2381–2398. <https://doi.org/10.1002/2016JF003869>
- 425 Mikkelsen, A. B., Hubbard, A., MacFerrin, M., Box, J. E., Doyle, S. H., Fitzpatrick, A., Hasholt, B., Bailey, H. L.,
426 Lindbäck, K., & Pettersson, R. (2016). Extraordinary runoff from the Greenland ice sheet in 2012 amplified by
427 hypsometry and depleted firn retention. *The Cryosphere*, 10(3), 1147–1159. <https://doi.org/10.5194/tc-10-1147-2016>
- 428 Miller, J. Z., Culberg, R., Long, D. G., Shuman, C. A., Schroeder, D. M., & Brodzik, M. J. (2022). An empirical
429 algorithm to map perennial firn aquifers and ice slabs within the Greenland Ice Sheet using satellite L-band
430 microwave radiometry. *The Cryosphere*, 16(1), 103–125. <https://doi.org/10.5194/tc-16-103-2022>
- 431 Nghiem, S. V., Hall, D. K., Mote, T. L., Tedesco, M., Albert, M. R., Keegan, K., Shuman, C. A., DiGirolamo, N. E.,
432 & Neumann, G. (2012). The extreme melt across the Greenland ice sheet in 2012. *Geophysical Research Letters*,
433 39(20), 2012GL053611. <https://doi.org/10.1029/2012GL053611>
- 434 Pfeffer, W. T., & Humphrey, N. F. (1998). Formation of ice layers by infiltration and refreezing of meltwater.
435 *Annals of Glaciology*, 26, 83–91. <https://doi.org/10.3189/1998AoG26-1-83-91>
- 436 Pfeffer, W. T., Meier, M. F., & Illangasekare, T. H. (1991). Retention of Greenland runoff by refreezing:
437 Implications for projected future sea level change. *Journal of Geophysical Research*, 96(C12), 22117.
438 <https://doi.org/10.1029/91JC02502>
- 439 Rennermalm, Å. K., Hock, R., Covi, F., Xiao, J., Corti, G., Kingslake, J., Leidman, S. Z., Miège, C., MacFerrin, M.,
440 Machguth, H., Osterberg, E., Kameda, T., & McConnell, J. R. (2021). Shallow firn cores 1989–2019 in southwest
441 Greenland's percolation zone reveal decreasing density and ice layer thickness after 2012. *Journal of Glaciology*,
442 68(269), 431–442. <https://doi.org/10.1017/jog.2021.102>
- 443 Rignot, E., Box, J. E., Burgess, E., & Hanna, E. (2008). Mass balance of the Greenland ice sheet from 1958 to 2007.
444 *Geophysical Research Letters*, 35(20), L20502. <https://doi.org/10.1029/2008GL035417>
- 445 Rignot, E., & Mouginot, J. (2012). Ice flow in Greenland for the International Polar Year 2008-2009: ICE FLOW
446 GREENLAND 2009. *Geophysical Research Letters*, 39(11), n/a-n/a. <https://doi.org/10.1029/2012GL051634>
- 447 Rodriguez-Morales, F., Byers, K., Crowe, R., Player, K., Hale, R. D., Arnold, E. J., Smith, L., Gifford, C. M.,
448 Braaten, D., Panton, C., Gogineni, S., Leuschen, C. J., Paden, J. D., Li, J., Lewis, C. C., Panzer, B., Gomez-Garcia
449 Alvestegui, D., & Patel, A. (2014). Advanced Multifrequency Radar Instrumentation for Polar Research. *IEEE*
450 *Transactions on Geoscience and Remote Sensing*, 52(5), 2824–2842. <https://doi.org/10.1109/TGRS.2013.2266415>
- 451 Rodriguez-Morales, F., Gogineni, P., Leuschen, C., Allen, C., Lewis, C., Patel, A., Byers, K., Smith, L., Shi, L.,
452 Panzer, B., Blake, W., Crowe, R., & Gifford, C. (2010). Development of a multi-frequency airborne radar
453 instrumentation package for ice sheet mapping and imaging. *2010 IEEE MTT-S International Microwave*
454 *Symposium*, 157–160. <https://doi.org/10.1109/MWSYM.2010.5518197>

- 455 Samimi, S., Marshall, S. J., & MacFerrin, M. (2020). Meltwater Penetration Through Temperate Ice Layers in the
456 Percolation Zone at DYE-2, Greenland Ice Sheet. *Geophysical Research Letters*, 47(15).
457 <https://doi.org/10.1029/2020GL089211>
- 458 Tedesco, M., & Fettweis, X. (2020). Unprecedented atmospheric conditions (1948–2019) drive the 2019 exceptional
459 melting season over the Greenland ice sheet. *The Cryosphere*, 14(4), 1209–1223. [https://doi.org/10.5194/tc-14-](https://doi.org/10.5194/tc-14-1209-2020)
460 1209-2020
- 461 Tedesco, M., Fettweis, X., Mote, T., Wahr, J., Alexander, P., Box, J. E., & Wouters, B. (2013). Evidence and
462 analysis of 2012 Greenland records from spaceborne observations, a regional climate model and reanalysis data. *The*
463 *Cryosphere*, 7(2), 615–630. <https://doi.org/10.5194/tc-7-615-2013>
- 464 Tedesco, M., Fettweis, X., van den Broeke, M. R., van de Wal, R. S. W., Smeets, C. J. P. P., van de Berg, W. J.,
465 Serreze, M. C., & Box, J. E. (2011). The role of albedo and accumulation in the 2010 melting record in Greenland.
466 *Environmental Research Letters*, 6(1), 014005. <https://doi.org/10.1088/1748-9326/6/1/014005>
- 467 Tedstone, A. J., & Machguth, H. (2022). Increasing surface runoff from Greenland's firn areas. *Nature Climate*
468 *Change*. <https://doi.org/10.1038/s41558-022-01371-z>
- 469 The IMBIE Team. (2020). Mass balance of the Greenland Ice Sheet from 1992 to 2018. *Nature*, 579(7798), 233–
470 239. <https://doi.org/10.1038/s41586-019-1855-2>
- 471 van Angelen, J. H., van den Broeke, M. R., Wouters, B., & Lenaerts, J. T. M. (2014). Contemporary (1960–2012)
472 Evolution of the Climate and Surface Mass Balance of the Greenland Ice Sheet. *Surveys in Geophysics*, 35(5),
473 1155–1174. <https://doi.org/10.1007/s10712-013-9261-z>
- 474 van As, D., Fausto, R. S., Cappelen, J., van de Wa, R. S. W. I., Braithwaite, R. J., Machguth, H., & PROMICE
475 project team, *. (2016). Placing Greenland ice sheet ablation measurements in a multi-decadal context. *GEUS*
476 *Bulletin*, 35, 71–74. <https://doi.org/10.34194/geusb.v35.4942>
- 477 van den Broeke, M. R., Enderlin, E. M., Howat, I. M., Kuipers Munneke, P., Noël, B. P. Y., van de Berg, W. J., van
478 Meijgaard, E., & Wouters, B. (2016). On the recent contribution of the Greenland ice sheet to sea level change. *The*
479 *Cryosphere*, 10(5), 1933–1946. <https://doi.org/10.5194/tc-10-1933-2016>
- 480 Vandecrux, B., MacFerrin, M., Machguth, H., Colgan, W. T., van As, D., Heilig, A., Stevens, C. M., Charalampidis,
481 C., Fausto, R. S., Morris, E. M., Mosley-Thompson, E., Koenig, L., Montgomery, L. N., Miège, C., Simonsen, S. B.,
482 Ingeman-Nielsen, T., & Box, J. E. (2019). Firn data compilation reveals widespread decrease of firn air content in
483 western Greenland. *The Cryosphere*, 13(3), 845–859. <https://doi.org/10.5194/tc-13-845-2019>

1



2

3

[Geophysical Research Letters]

4

Supporting Information for

5

Greenland Ice Sheet ice slab expansion and thickening

6

N. Jullien¹, A. J. Tedstone¹, H. Machguth¹, N. B. Karlsson², V. Helm³

7

¹Department of Geosciences, University of Fribourg, Fribourg, Switzerland

8

²Geological Survey of Denmark and Greenland, Copenhagen, Denmark

9

³Alfred Wegener Institute, Helmholtz Centre for Polar and Marine Sciences, Bremerhaven, Germany

10

11 Contents of this file

12

Text S1 to S4

13

Figures S1 to S12

14

Tables S1 to S3

15

16 Introduction

17

In the following we provide additional information on the processing and interpretation of accumulation radar data in 2002-03 and 2010-18. We provide additional figures that are discussed in the main manuscript as well as in text S1, S2, S3 and S4.

18

19

20

21 **Text S1. Ice content identification in 2002-2003**

22 Dataset preparation

23 We downloaded all accumulation radar (AR) data acquired over the GrIS. We added
24 coordinates to each radargram by matching the timestamps from the radargram with
25 those provided in the flight path dataset. Radargrams were detrended in the logarithmic
26 domain by the provider (J. Paden, personal communication 2020). We refer to the data in
27 the radargrams as 'signal strength', in the unit of decibels.

28 Surface picking

29 We picked the ice sheet surface following the approach used by MacFerrin et al. (2019).
30 First, we manually identified the surface at the start of each radargram. Then, for each
31 trace in the radargram, the surface identification uses a vertical 100-pixel 3-standard
32 deviation pseudo-Gaussian kernel mask over a 40 vertical pixels search window (150
33 vertical pixels search window in MacFerrin et al. (2019)), centered on the proposed
34 surface. The identified surface of that trace corresponds to the index of the largest value
35 from the convolution between the kernel mask and the radar signal in the search
36 window. The index of the identified surface is then used as a suggested surface in the
37 next trace, and so on until the end of the radargram is reached. When the algorithm
38 failed to identify the surface then we picked the surface manually. The surface picking
39 procedure was smoothed similarly to MacFerrin et al. (2019) by comparing the surface
40 slope in each trace with the average surface slope of the 10 preceding traces. If the slope
41 difference was larger than 5 vertical pixels or was 50% higher than the average slope of
42 the 10 preceding traces, we considered the 20 traces ahead and found the trace whose
43 slope is within 10% the mean slope of the 10 preceding traces. We then calculated the
44 surface location by linear interpolation between the surface pixel before the jump and
45 the next matching trace. We inspected all resulting surface picks manually.

46 As the firn column is considered to be dry during the springtime airborne radar
47 campaigns, we used the speed of the electromagnetic signal through refrozen ice within
48 firn derived by MacFerrin et al. (2019) to retrieve depth in each radargram. For further

49 details on the discussion of the speed of the electromagnetic signal in such a medium,
50 we refer the reader to MacFerrin et al., (2019).

51 Ice content identification

52 We identified ice content via expert manual classification of the uppermost 30 m of each
53 radargram. Each radargram was inspected using a histogram stretch between the 2.5%
54 and 97.5% percentiles of the radar signal strength distribution from all the radargrams of
55 the corresponding year. As these data have been detrended in the logarithmic domain
56 we are limited to quantifying ice layer and slab extent only, leaving thickness estimates
57 possible only occasionally.

58 Depending on the surface regime (i.e. ablation zone, percolation zone, dry snow zone),
59 different characteristic features can be identified within the subsurface. Fig. 1 shows four
60 radargrams (0-30 m) that represent different subsurface conditions. Radar returns in the
61 ablation zone (Fig. 1b) are uniform with no major variations in signal strength. The
62 percolation zone can show thin and sharp layering probably associated with decimeter-
63 scale ice layers (Fig. 1c), but can also show meters-thick layering probably associated
64 with ice slabs (Fig. 1d). The dry snow zone shows regular parallel layering associated with
65 annual snow accumulation (Fig. 1e).

66 We considered whether the signal in Fig. 1c,d was indicative of ice content. Besides ice
67 content, there are two other possibilities: (1) liquid water presence, and (2) wind-
68 hardened, buried surface layers. To check the likelihood of these two other possibilities,
69 we focus on a candidate radargram in SW Greenland (Fig. S1, similar to the one shown in
70 Fig. 1d) where layers several meters thick are thought to correspond to ice. Liquid water
71 was discounted as the return signal associated with liquid water shows typically a
72 mirroring (peak on the opposite side) of the signal compared to the signal peak related
73 to the surface (e.g. Fig. 18 in Karlsson et al. (2019)). This was not observed in the
74 candidate radargram (Fig. S1b-e). Furthermore, liquid water would blind the radar signal
75 below, but we do not see any evidence of this (Figs. 1d and S1b-e).

76 To investigate the possibility of a wind-hardened buried surface layer, we estimated the
77 thickness of annual snowpack accumulation. Fettweis et al. (2020) indicate that mean
78 annual snowfall ranges between 200 and 600 mm w. e. year⁻¹ with a spread of 0-150
79 mm w. e. year⁻¹ in the area of interest. This gives a low and high end of yearly snowfall of
80 50-750 mm w. e. year⁻¹. Considering a firn density of 500 kg · m⁻³ (Braithwaite et al.,
81 1994) yields a plausible range of 0.1 to 1.5 m thickness for each buried surface layer. As
82 the layers in the radargram are several meters thick it is therefore unlikely that the signal
83 corresponds to a wind-hardened buried layer and so we conclude that the return signal
84 is associated with ice slabs. We interpret thinner layers as indicative of ice layers (see thin
85 layering in Fig. 1c).
86

87 **Text S2. Ice content identification from 2010 to 2018**

88 With radar data acquired during 2010 to 2018 we had two goals: first, to identify
89 changing ice slab extent for comparison to the extents found in the 2002-03 period, and
90 second, to quantify changes in slab thickness. This second goal required us to be able to
91 quantitatively compare successive radargrams, necessitating a rigorous semi-automated
92 approach to ice content identification.

93 Dataset preparation

94 We identified ice slabs in the L1B radargrams collected by the Accumulation Radar (AR)
95 within NASA's Operation IceBridge following a similar approach to MacFerrin et al.
96 (2019). We reprocessed the same 2010-2014 data as were used by MacFerrin et al.
97 (2019). To identify ice slabs in data acquired during 2017 and 2018, we applied a
98 location-based matching between the new radargrams and the 2010-2014 ice slabs
99 extent found by MacFerrin et al. (2019). We retained all coincident radargrams as well as
100 the ones in the vicinity of the ice slabs extent to ensure any changes in the subsurface
101 firn near the pre-existing ice slabs would be identified. We applied a logarithmic
102 transformation to the L1B radargrams (but did not multiply it by 10 as in Carl et al.,
103 (2011)) and refer to this as the 'signal strength' of the radargram, in the unit of decibels.

104 Surface picking and defining exclusions

105 From the log-transformed radargrams we picked the surface of the ice sheet following
106 the approach used by MacFerrin et al. (2019) (Fig. S2a) . For 2017-2018 data, we
107 manually identified the surface of the ice sheet at the start of each radargram and
108 provided it to the algorithm. We then applied the surface pick to the radargram (Fig.
109 S2b) and extracted the uppermost 100 m in order to carry out the corrections procedure
110 outlined in the next step. We manually excluded areas with lakes and other obvious
111 artefacts (i.e. signal failure) (Fig. S2c).

112 Correction for aircraft roll and signal attenuation with depth

113 We corrected the radar signal strength for the roll of the aircraft following MacFerrin et
114 al. (2019) (Fig. S2d). On occasion, the roll correction failed, which was noticeable by

115 signal return strengths remaining much lower than following a successful roll correction.
116 Such data were excluded from further analysis. In addition, much of the data collected in
117 2018 were affected by a periodicity artefact caused by the radar beam being steered off
118 nadir during data collection (J. Li, personal communication, 2021) which prevented roll
119 correction and made them ineligible for further analysis.

120 To ensure that radar signal strength returned from the subsurface would be comparable
121 between radargrams, we subtracted the average surface radar signal strength from the
122 sub-surface signal, thereby removing the majority of the atmospheric influences upon
123 the return signal (Fig. S2e) while retaining the physical dimension of the radar signal.
124 Finally, we corrected for depth attenuation of the radar signal following a slightly
125 modified version from MacFerrin et al. (2019) (we did not apply variance normalisation)
126 (Fig. S2f), and clipped each radargram to the uppermost 30 m corresponding to the
127 depth range which is expected to contain ice slabs in order to simplify later processing
128 steps.

129 Re-scaling of radar signal

130 Fourteen of the 448 radargrams (3%) displayed little variation in their return signal,
131 making it difficult to identify ice slabs. We therefore rescaled these depth-corrected
132 radargrams by applying a histogram stretch using the 5th and 95th percentiles from the
133 combined distribution of the other depth-corrected radargrams.

134 Initial comparison with MacFerrin et al., (2019)

135 Initially, we reprocessed the 2010-14 data using the same ice identification algorithm as
136 MacFerrin et al. (2019). They used a relative threshold unique to each radargram to
137 identify ice slabs in the uppermost 20 m, but we found that this approach did not reliably
138 return identical ice features between individual successive radargrams. Hence, the
139 original algorithm is not well-suited to compare ice thickness across individual years. We
140 therefore developed a new algorithm to identify ice slabs in the uppermost 20 m, based
141 on the application of a universal range of radar signal strengths extracted from a
142 reference radargram.

143 Identification of ice content versus porous firn

144 **Identifying the return signal strength that is indicative of ice content.** We aimed to
145 identify the range of radar signal strengths that enables differentiation between porous
146 firn versus ice content across the entire dataset. In 2013, MacFerrin et al. (2019) collected
147 in-situ ground penetrating radar data and firn cores coincident with an Operation
148 IceBridge AR radargram during the same spring, which they used to validate the
149 identification of ice slabs in airborne radar data. Here, we adopt this AR radargram as our
150 “reference radargram” (see Fig. S3a).

151 We manually identified ice slabs in the depth-corrected AR reference radargram (Fig.
152 S3b), referred as in-situ ice content. We adopted a conservative approach, seeking to
153 include ice which was positively identified in ground-based in-situ GPR data by
154 MacFerrin et al., (2019), easily distinguishable from porous firn, and continuous. Next, we
155 used this mask to extract the distributions of signal strength from the reference
156 radargram for (a) porous firn and (b) ice content (Fig. S4). The overlap in the signal return
157 strength between the two facies means that a single threshold to fully differentiate
158 porous firn and ice content cannot be defined. Instead, we developed an algorithm using
159 a range of thresholds based on the quantiles of the ice content signal distribution to
160 distinguish between ice content and porous firn.

161 Fig. S3c illustrates the performance of the new algorithm on the reference radargram in
162 detecting ice content for quantile 0.65 of the ice content distribution (our lower
163 threshold), and Fig. S3d for quantile 0.79 (our upper threshold). Quantile 0.65 is the
164 highest quantile for which the algorithm correctly identifies ice without erroneously
165 including firn (see Tab. S1), at the cost of missing some ice content (see Fig. S3c). Above
166 this threshold, some areas that have been mapped to be porous firn start to be falsely
167 identified as ice. These facies correspond to an intermediate state between porous firn
168 and ice slabs (see Fig. 2b,c in MacFerrin et al. (2019)), most likely several ice layers within
169 firn. By quantile 0.80 (not shown), porous firn unlikely to contain numerous ice layers
170 starts to be identified as ice. We therefore applied thresholds in the quantile range 0.65

171 to 0.79 from the ice content distribution to detect ice presence. We discuss accuracy
172 further below.

173 **Extracting ice content.** For each radargram, we extracted ice content across the range
174 of thresholds described above in 0.01 increments, corresponding to retrievals at 15
175 individual thresholds. Following MacFerrin et al. (2019), we removed small-scale noise by
176 applying a filter to each ice content retrieval to remove small individual ice features 1-2
177 pixels wide, and a continuity threshold to retain only pixels which were spatially
178 continuously connected to at least 350 other pixels. We show the resulting ice content
179 identification for quantile 0.65 in Fig. S2h and quantile 0.79 in Fig. S2i. The ice features
180 identified in each individual quantile is referred to ice slabs.

181 **Ice content likelihood.** We computed an ice content likelihood for each radargram as
182 the percentage of the 15 different levels of ice content in which each pixel was identified
183 as containing ice (Fig. S2g).

184 **Post-processing and verification.** In some radargrams we found that some porous firn
185 areas were wrongly identified as ice, probably because of the significant overlap of the
186 two distributions (Fig. S4). We therefore manually excluded these areas from the final
187 results (Fig. S2j). The list of exclusions is provided in the code repository.

188 Accuracy assessment

189 We considered the accuracy of the extreme end members of the quantile range (quantile
190 0.65 and quantile 0.79). Tables S1 and S2 show the two contingency tables given by
191 quantiles 0.65 and quantile 0.79 with respect to the in-situ ice content. As could be
192 expected from the ice content and porous firn signal strength distributions (Fig. S4), a
193 lower threshold quantile performs better in correctly identifying porous firn but performs
194 less well in correctly identifying ice. Conversely, a higher threshold quantile performs
195 better in identifying ice compared to a lower threshold but at the cost of a poorer
196 performance in correctly identifying porous firn. Overall, the total accuracy is higher for
197 the highest quantile.

198 Ice slab extent

199 As described in the main text, we defined ice slabs as present in areas with at least 1 m
200 of subsurface ice content by the end of the study period. Following MacFerrin et al.
201 (2019), we only mapped ice slabs above the long-term ELA (i.e. where firn exists), and so
202 our lower ice slabs bounds match theirs.

203 Final comparison with MacFerrin et al. (2019)

204 At higher elevations, our ice slab identification yielded some differences with the
205 identification by MacFerrin et al. (2019). Indeed, inspection of individual radargrams
206 revealed that MacFerrin et al. (2019) incorrectly identified ice slabs in some areas,
207 especially in the NE towards the high boundary. As a result, our final ice slab extent
208 differs slightly from MacFerrin et al. (2019). The largest differences are found in the NW,
209 NO and NE (Fig. S12). For example, our 2010-2018 upper ice slabs limit extends less
210 inland compared to the 2010-2014 extent from MacFerrin et al., (2019) in-between
211 upstream of Petermann glacier and Qaanaaq Mitarfik (Thule Air Base) in the NW and NO.
212 The similar is observed upstream of Nioghalvfjærdsbrae (79 N Glacier) in the NE. Overall,
213 MacFerrin et al., (2019) estimated ice slabs extended over 64'800-69'400 km² in 2014; we
214 find ice slabs extended over 60'400-73'500 km² in 2018.

215 **Text S3. Distinction between, 'in-initiation', 'in-development' and 'well-**
216 **developed' ice slabs**

217 We analyze the ice content change from the start to the end of the studied period. We
218 identify three stages in ice slab development corresponding to their changes in
219 thickness:

- 220 i. In the 'in-initiation' stage, the firm was free of ice slabs at the start of the studied
221 period, and had developed new ice slabs by the end of the studied period.
- 222 ii. In the 'in-development' stage, ice slabs experienced substantial (metres)
223 thickening during the studied period.
- 224 iii. In the 'well-developed' stage, the thickness of the ice slab was already large (i.e.
225 larger than 10 m thick) at the start of the studied period; its thickness often
226 increased further during the studied period.

227 In Fig. S5 we illustrate these different categories by splitting transect F (Fig. 3f) into
228 corresponding sectors. Note that we did not set the maximum boundary of ice thickness
229 to be 16m for this analysis; ice thickness can thus reach 20 m.

230 In the "well-developed" sector, the median ice content stayed roughly the same in 2017
231 compared to 2010 (14 m and 15 m respectively) (Fig. S5b), with negligible overall change
232 (-2% in 2017 compared to 2010) (Fig. S5e).

233 In the "in-development" sector, the median ice content increased from 4.2 m to 11.5 m
234 (Fig. S5c, see also the quantiles 0.25 and 0.75 in Table S3), equivalent to an increase of
235 194% from 2010 to 2017 (Fig. S5f).

236 In the "in-initiation" sector, no ice slab was identified in 2010, but a new ice slab had
237 developed by 2017 (Fig. S5g) whose median ice content was 5 m in 2017 (Fig. S5d).

238 We performed the same analysis for transects C and D (Fig. 3c,d) and we present the
239 results in Table S3. We conclude similar patterns as in transect F are taking place in
240 transects C and D.

241 **Text S4. Ice accretion**

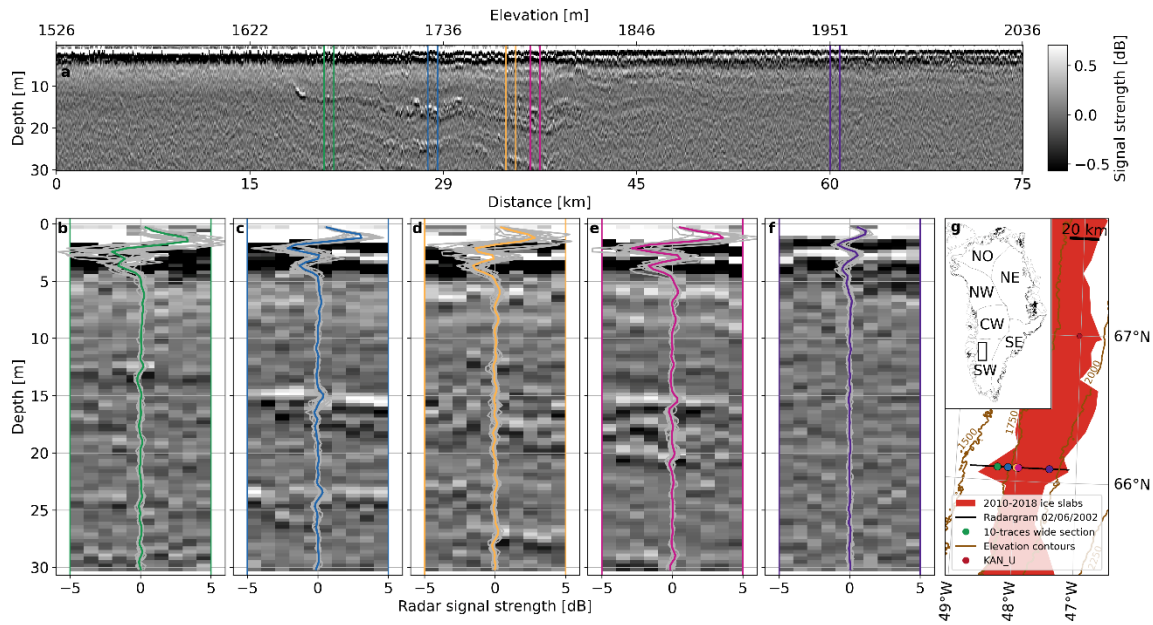
242 We differentiate between top-down ice accretion versus accretion on the undersides of
243 ice slabs (Fig. 4d). From spring 2012 to spring 2018, both top-down and underside
244 accretion took place, which is clearly identifiable once it has been separated from lateral
245 and vertical displacement of the ice slab.

246 (i) **Lateral displacement:** Using local surface velocities measured from 2009 to
247 2013, we estimate that the ice was displaced laterally by ~312 m (Doyle et al.,
248 (2014)). This agrees well with the ~360 m that we estimate by comparing the
249 distribution of ice content located between 15.93 and 16.52 km in 2012 with
250 its corresponding location in 2018.

251 (ii) **Vertical displacement:** The bottom of the “double-layered” ice slab (from
252 13.8 to 15.6 km) in 2012 was found to be roughly 2.6 m lower by 2018, while
253 the ice slab from 16.5 to 17.7 km was found 3m deeper (Fig. 4d). This
254 apparent movement is due to subsequent accumulation. We estimated the
255 burial of the ice slab bottom from 2012 to 2018 using ice cores collected
256 previously (Rennermalm et al., (2021)). Due to extreme melting in summer
257 2012 (Fig. S6), the ice slab surface was exposed (Machguth et al., 2016),
258 meaning that any firn pore space remaining from 2011-12 accumulation was
259 minimal or non-existent. We were therefore able to estimate the lower
260 boundary of the ice slab at KAN_U in 2013 and 2017, concluding that the
261 bottom of the thick ice slab that developed in summer 2012 was buried by
262 roughly 1.7 m from 2013 to 2017. We lack cores from 2018 and thus cannot
263 estimate potential firn replenishment from spring 2017 to spring 2018.
264 Nevertheless, this estimate of 1.7 m burial between 2013 and 2017 seems a
265 reasonable lower bound approximation for 2012-2018 firn replenishment.

266 (iii) **Top-down accretion** took place on top of the slab, thickening the ice slab by
267 2.9 m from 2012 to 2018 in-between 16.5 and 17.7 km (Fig. 4d).

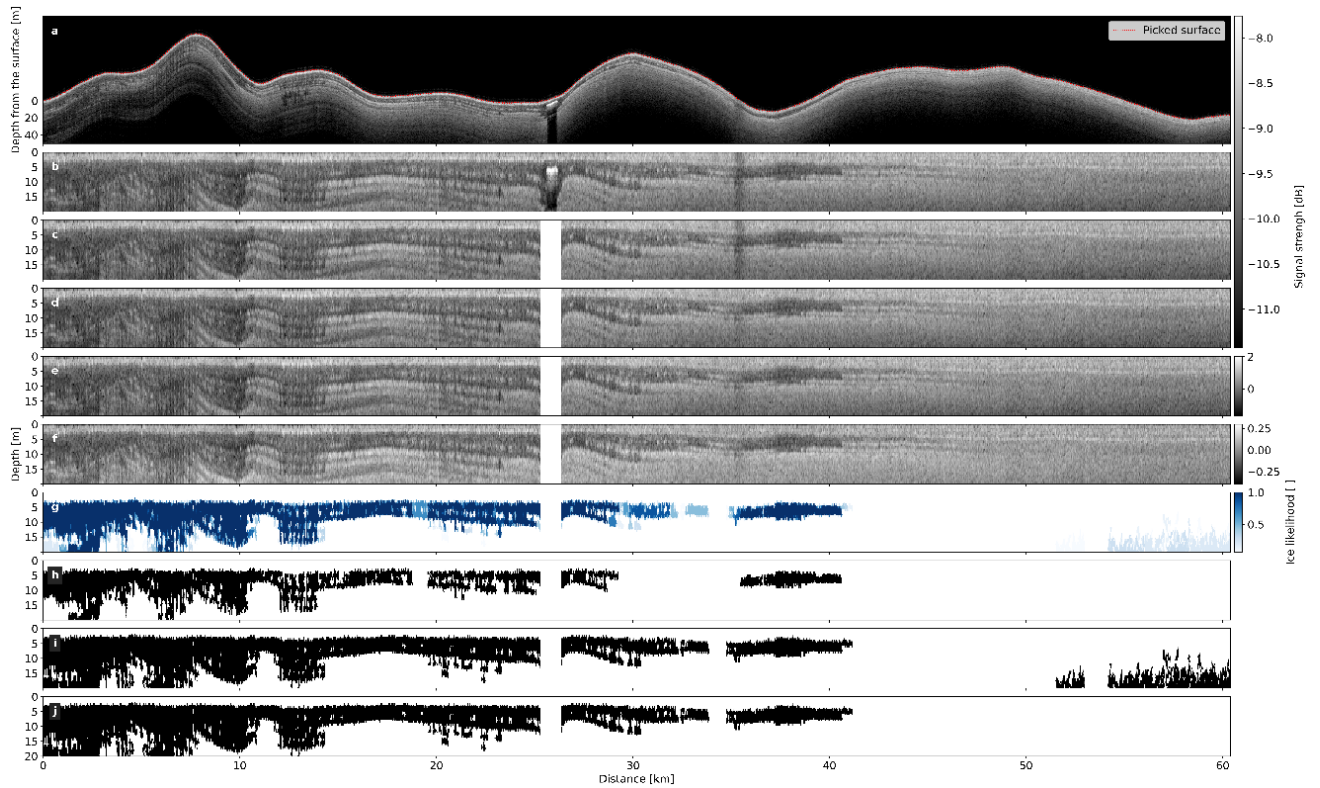
268 (iv) **Ice accretion on the undersides of ice slab** also occurred between 2012 and
269 2018 between 13.8 and 15.6 km, commencing at 11-13 m below the surface
270 and extending to 20 m deep (Fig. 4d).
271



272

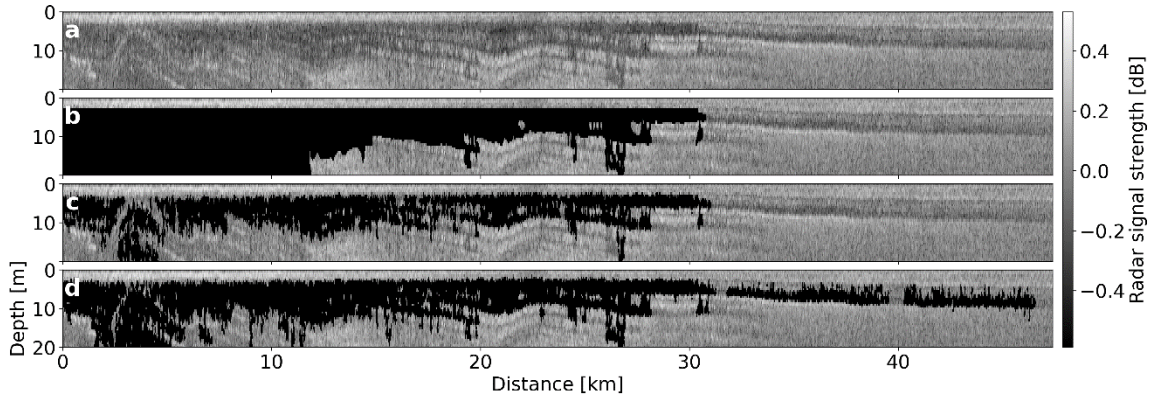
273 **Figure S1. Examples of ice content in 2003-03 data.** (a) Radargram acquired in SW
 274 Greenland on June 2nd, 2002 (background) and 10-traces wide limits of radar signal
 275 strength with color coding corresponding to panels b-f. (b-f) Individual trace signal
 276 profile (grey lines), average over the 10 traces of interest (color), and 10-traces
 277 radargram on the background. (b) An ice layer at 12-13 m depth. (c) Ice slabs are present
 278 between 14 m and 17 m depth and between 23 m and 25 m depth, (d) between 10 m
 279 and 20 m depth and at 27m depth, (e) in-between 15-21 m depth as well as at 29 m
 280 depth. (f) Porous firn without ice layers nor slabs. (g) Location of radargram compared to
 281 2010-2018 ice slabs extent.

282



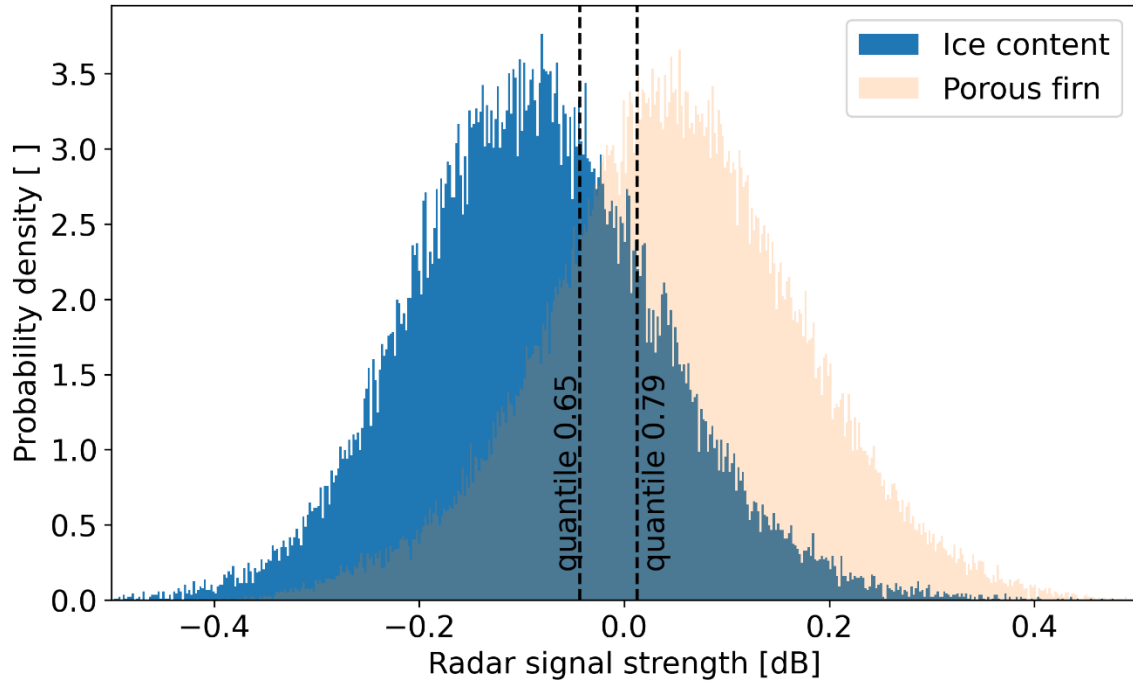
283

284 **Figure S2. Processing steps to identify ice content from airborne accumulation**
 285 **radar data**, illustrated using radargram 20140416_05_007_009. (a) raw airborne
 286 accumulation radar (AR) data before surface identification with the identified surface (red
 287 dotted line). (b) AR data after surface picking. (c) AR data after screening for areas to be
 288 excluded. (d) AR data after correction for the roll of the aircraft. (e) AR data after the
 289 removal of the average surface signal strength. (f) AR data after correction for the
 290 attenuation of the signal with depth. (g) Ice content likelihood, ranging from 0 to 1. (h)
 291 Ice content presence where each cell was mapped as ice at quantile 0.65. (i) Ice content
 292 presence where each cell was mapped as ice at quantile 0.79, corresponding to a
 293 likelihood of 1. (j) Final ice content at quantile 0.79, following manual porous firn
 294 exclusion.
 295



296

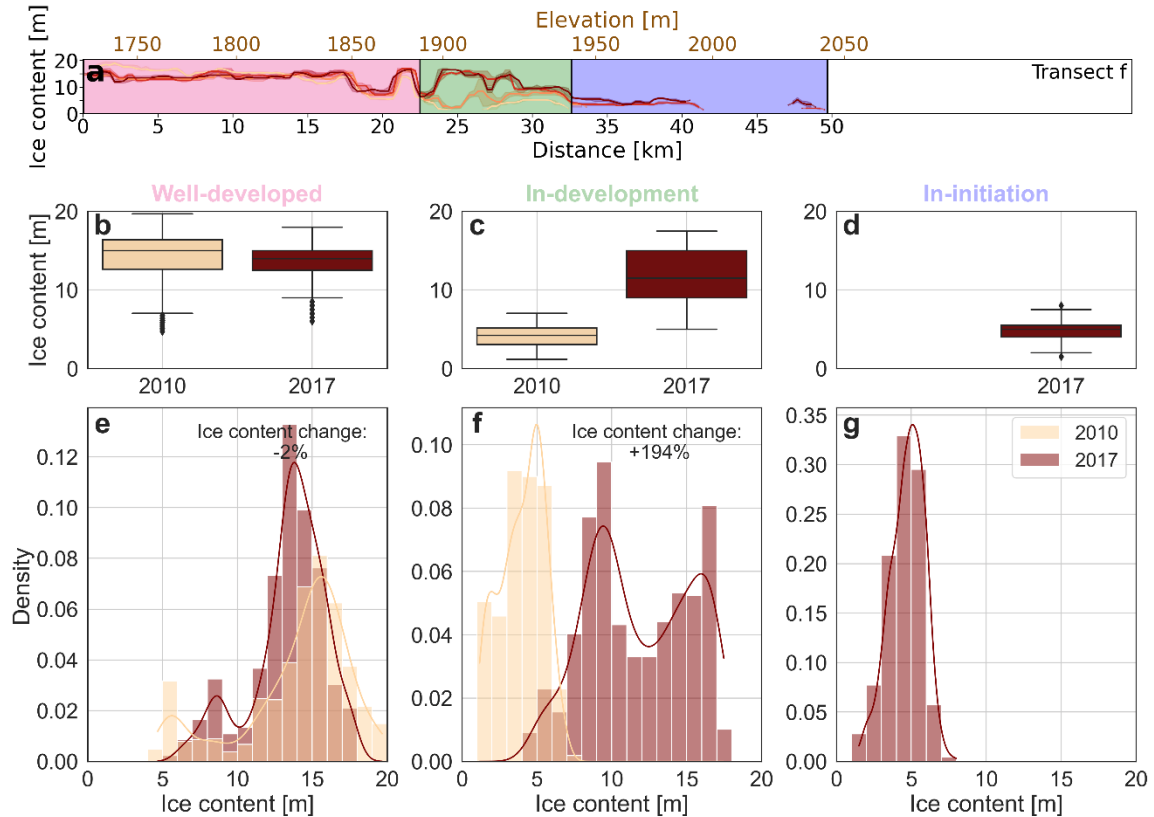
297 **Figure S3. Extraction of characteristic radar return strength from reference**
 298 **radargram.** (a-d) Depth corrected data for the reference radargram derived from AR
 299 data. (b) in-situ ice content mask (black). (c) Ice content retrieval using quantile 0.65 of
 300 the ice content distribution signal strength derived by applying the in-situ ice content
 301 mask (b) to the data in panel a. (d) As for panel c, using quantile 0.79.
 302



303

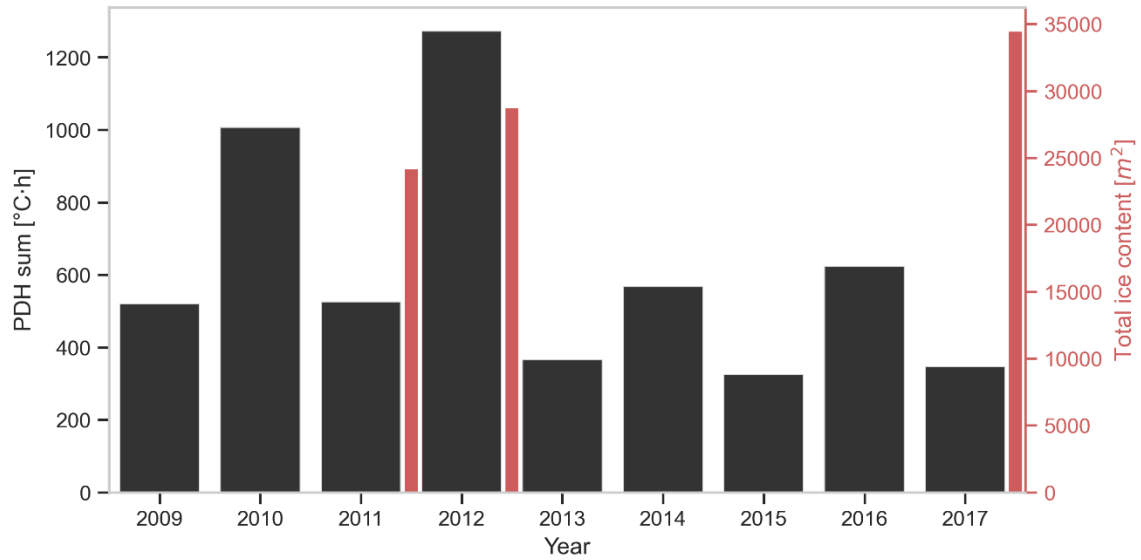
304 **Figure S4. Porous firn versus ice content signal strength distribution.** Calculated
 305 according to in-situ ice content in the depth-corrected reference radargram. The vertical
 306 dashed lines correspond to the quantile 0.65 and quantile 0.79 of the ice content
 307 distribution.

308



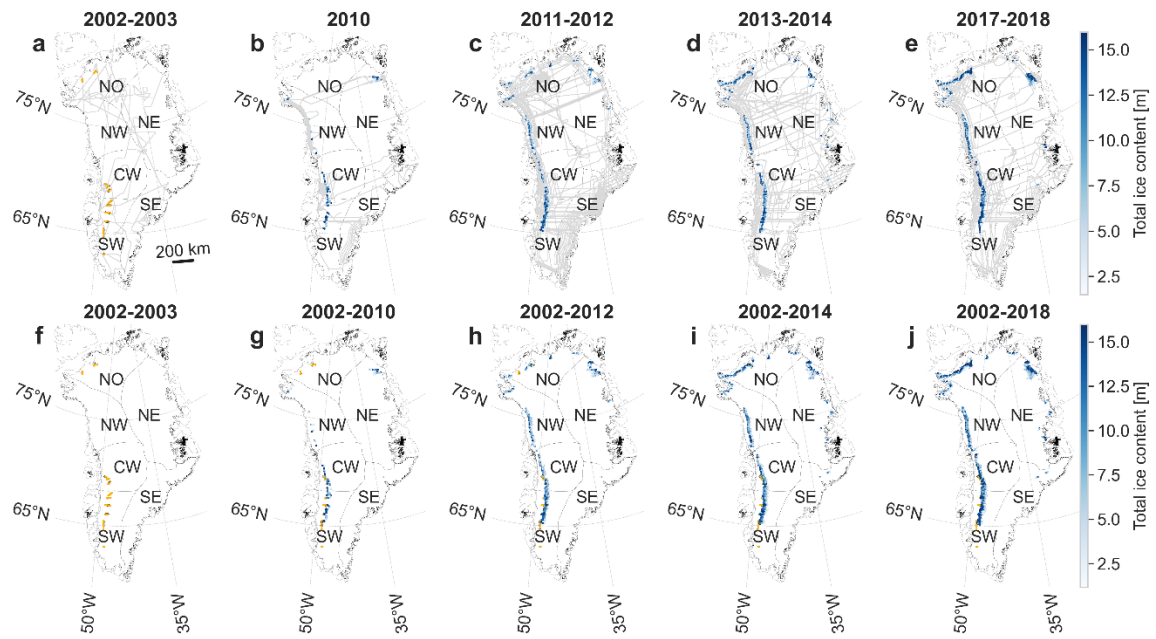
309
 310
 311
 312
 313
 314
 315
 316
 317
 318

Figure S5. Ice content change along transect F. (a) Ice content change from 2010 to 2017 (colored lines, same as in Fig. 3f) along the transect. The different sectors of changes in ice slabs thickness are indicated by the background shading: well-developed (pink), in-development (green), in-initiation (blue). (b-d) Boxplot of ice content in 2010 and 2017 in the three sectors. (e-f) Distribution of ice content in 2010 and 2017 in the three sectors. Lines denotes the kernel density estimate of the distributions. Percentage change indicate the relative change in total ice content in the sector of interest in 2017 compared to 2010.



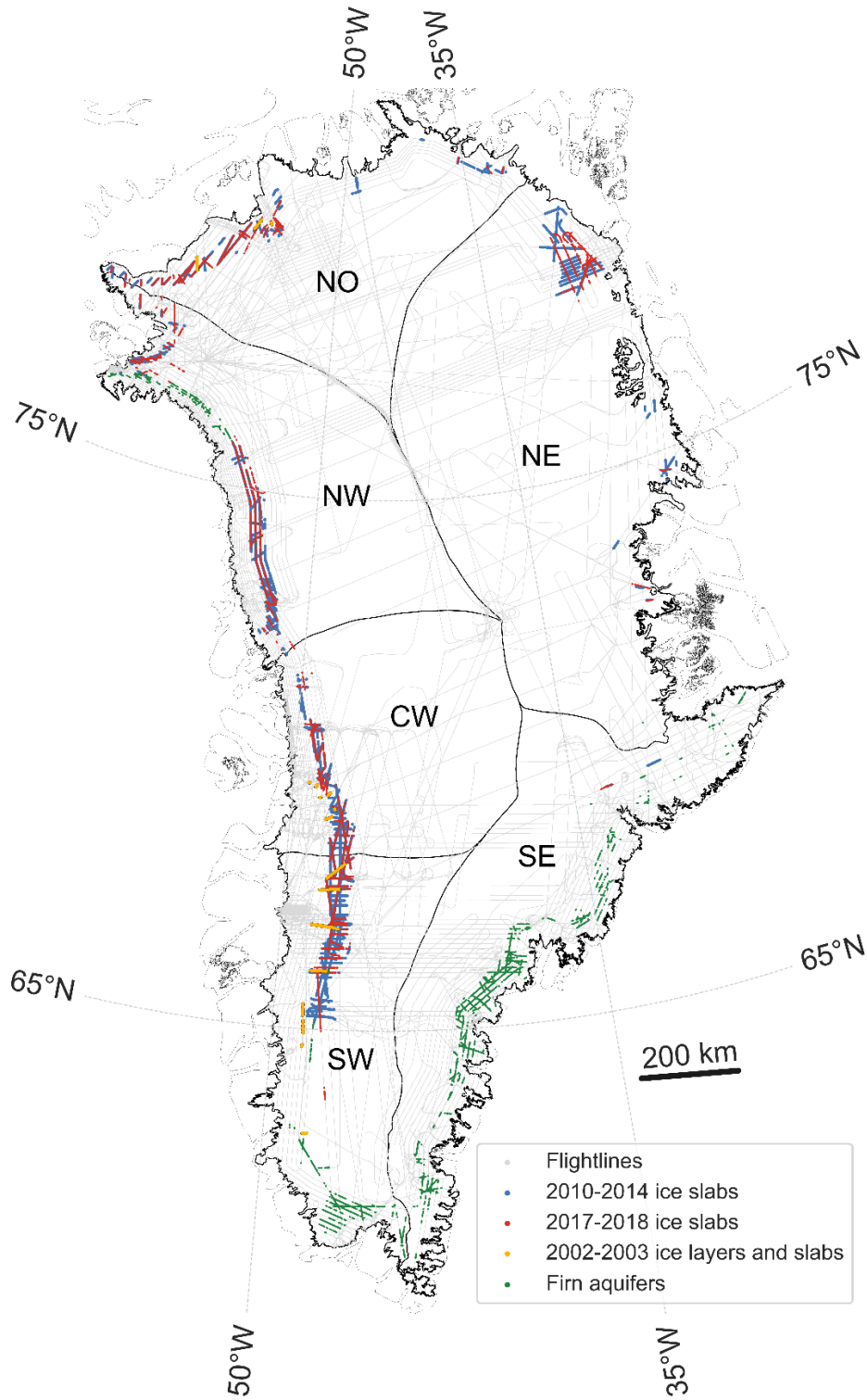
319
 320
 321
 322
 323

Figure S6. Melt potential at KAN_U. Positive Degree Hour sum [°C · h] during each summer (black) and total ice content according to radargrams each spring (red) within the area delimited by thick dashed lines in Fig. 4 (from 13.8 to 17.7 km).



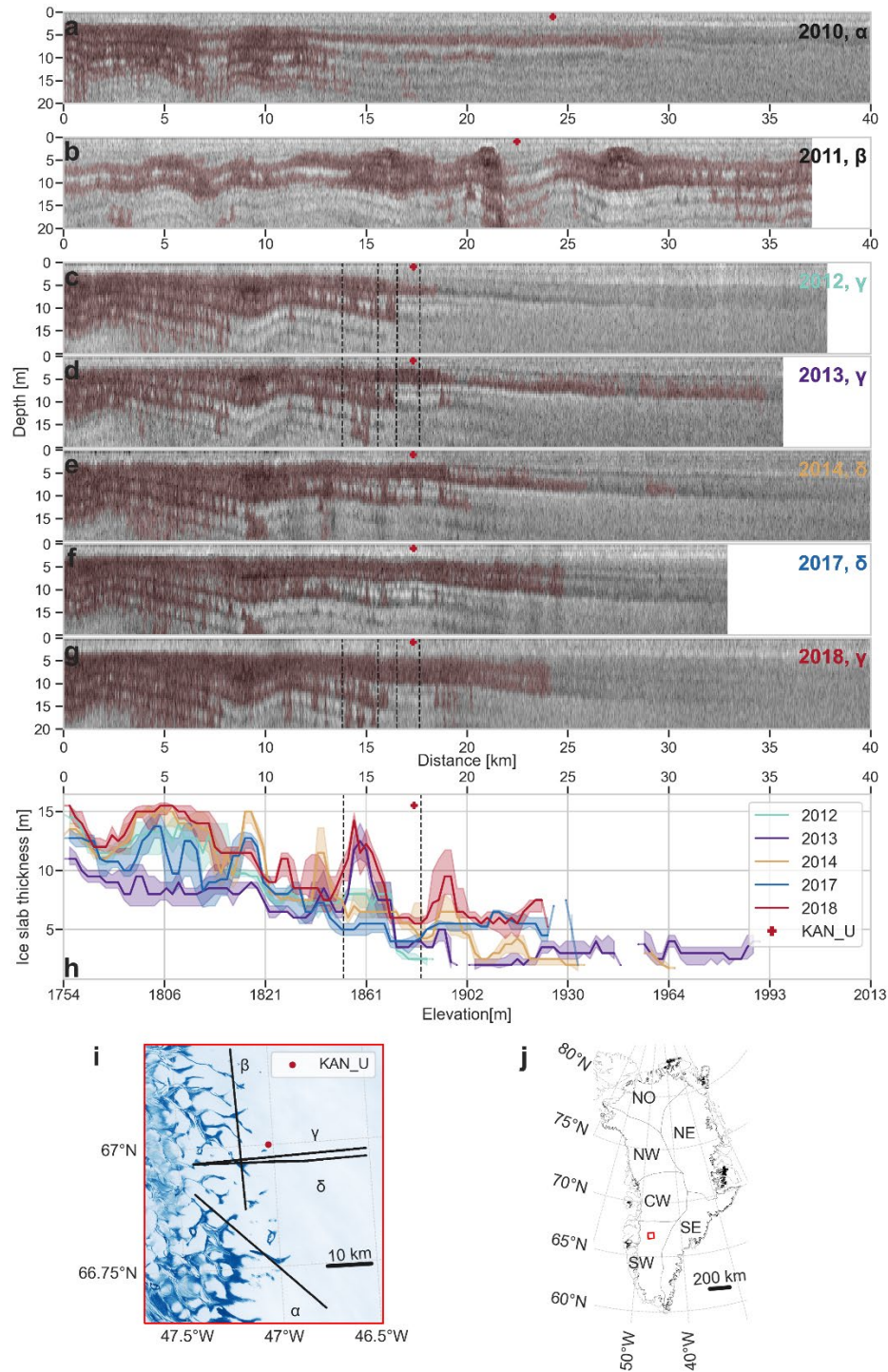
324
 325
 326
 327
 328

Figure S7. Ice slab mapping and growth over time. (a-e) Ice slabs mapped during each time period (color) and flight line (gray). (f-j) Cumulative ice slabs mapping (color) over successively longer time periods.

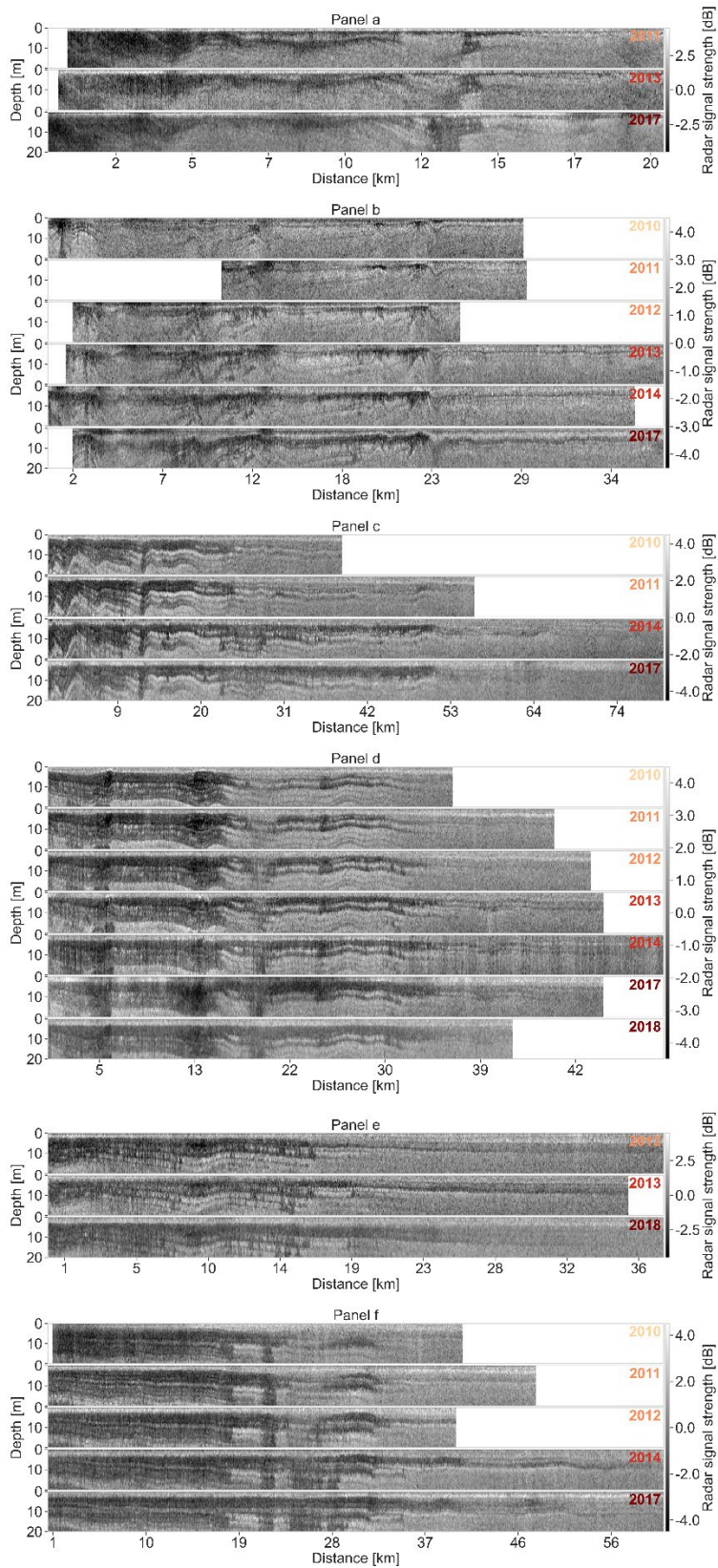


329
 330
 331
 332
 333
 334

Figure S8. Combined ice slab presence from 2002 to 2018. Ice layers and slabs mapped in 2002-03 (orange), 2010-14 (blue) and 2017-18 (red), firm aquifers in 2010-2014 (Miège et al., 2016) (green). Flight lines associated with 2002-2018 ice slabs are displayed in the background in grey.

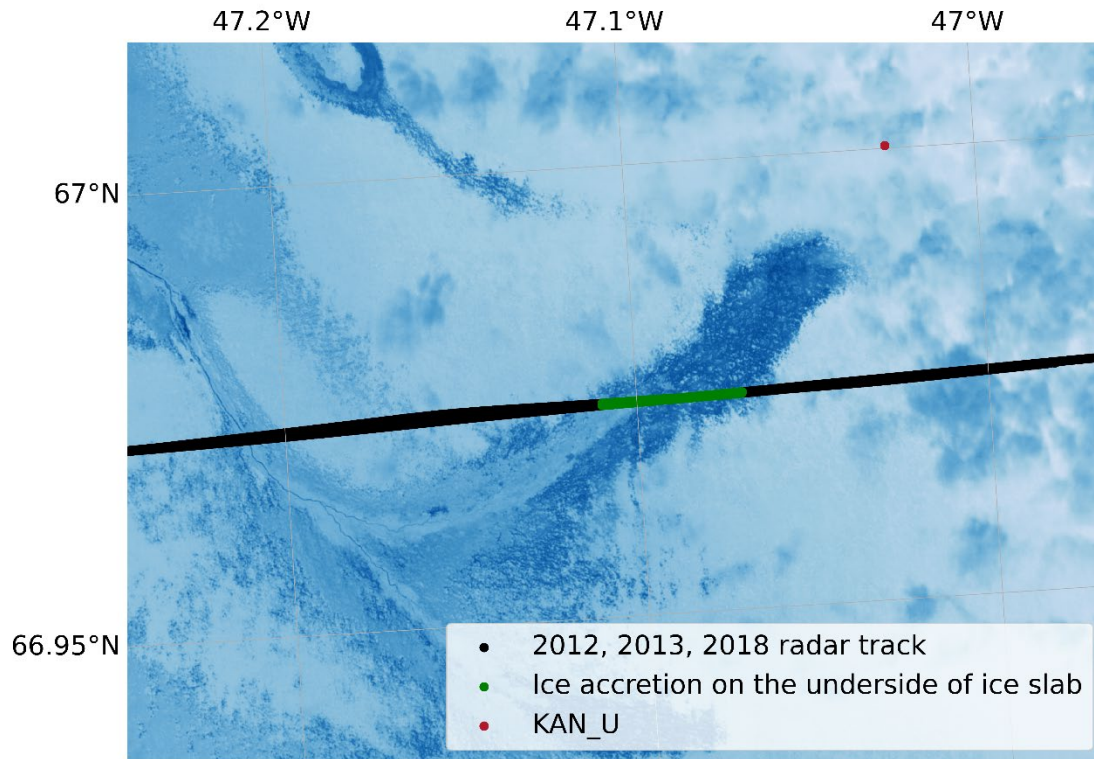


335
 336 **Figure S9. Ice thickness through time** along a transect close to KAN_U (red marker in
 337 each panel). (a-g) Radargrams in greyscale and resulting maximum likely ice content
 338 (quantile 0.79) in red. Dashed vertical lines delineate the areas discussed in the text. (h)
 339 Ice slab thickness in uppermost 20 m of radargrams (from 2012 onwards). Equivalent
 340 elevation (m above WGS84 ellipsoid) on lower x axis. (i) Near-infrared (band 8) Sentinel-2
 341 image acquired on August 23rd, 2021, with radargram locations. (j) Transect location on
 342 the GrIS (red square).



343

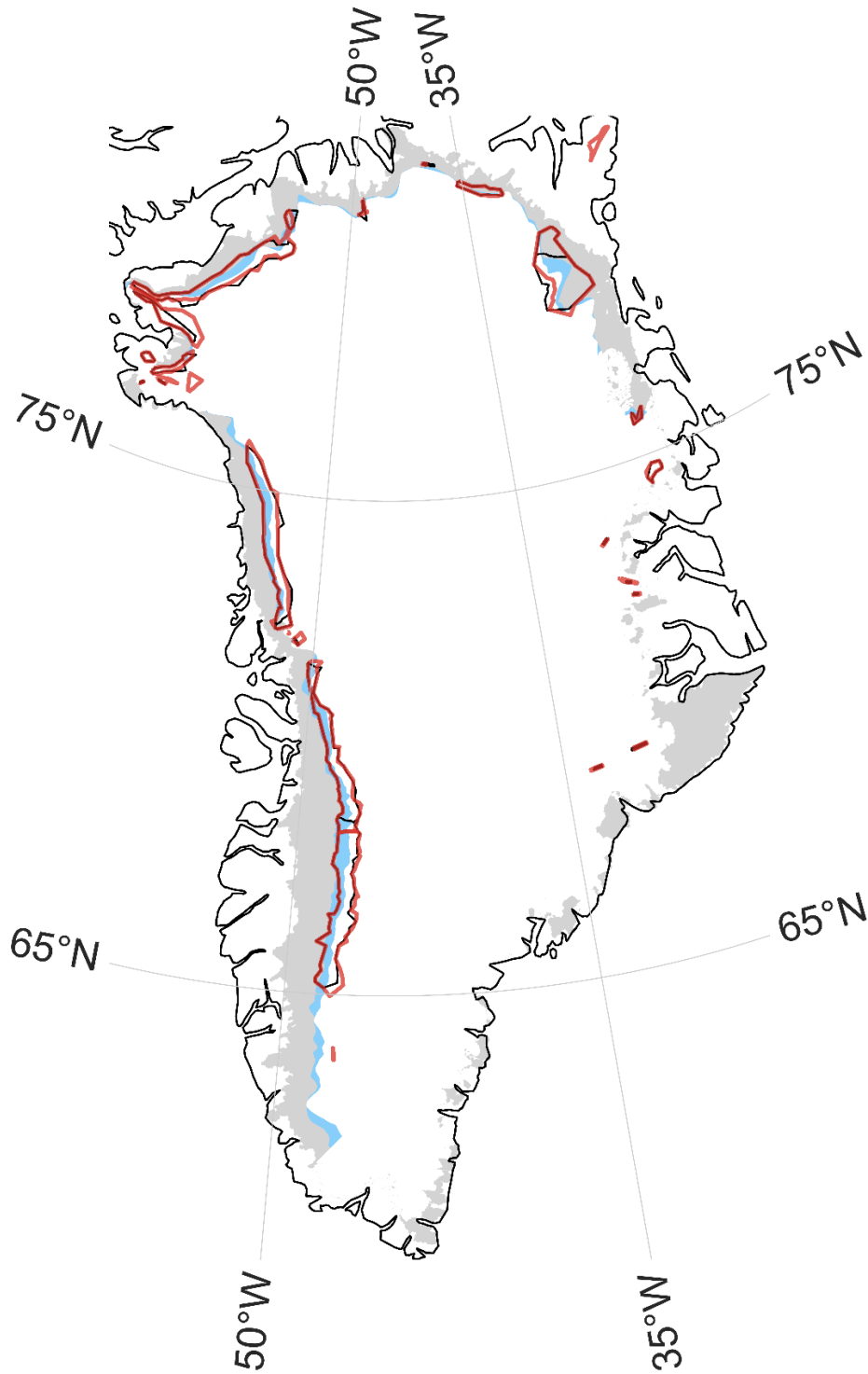
344 **Figure S10. Yearly radargrams of transects used in Fig. 3**



345

346 **Figure S11. Coincident surface hydrology and ice slab accretion.** Near-infrared (band
 347 8) Sentinel-2 image acquired on August 24th, 2016. Dark blue corresponds to slush
 348 fields. A developed hydrological network is seen in the lower left. Clouds are visible in
 349 the upper right. Radargrams (black) acquired in 2012, 2013 and 2018 (same as Fig. 4b,d).
 350 Radargrams with ice accretion on the underside of ice slab (green) identified by
 351 comparing 2012 with 2013 and 2018 radargrams (13.8 to 15.6 km in Fig. 4). KAN_U is
 352 indicated by the red dot.

353



354
 355
 356
 357
 358
 359
 360

Figure S12. Comparison between visible surface runoff area and ice slab extent. Visible surface runoff area in 1985-1992 (grey shading) and expansion in 2013-2020 (blue shading) from Tedstone & Machguth (2022). Ice slabs extent in 2010-2014 from MacFerrin et al. (2019) (black). Ice slabs extent at quantile 0.79 in 2010-2018 in this study (red).

	Firn (Q 0.65)	Ice (Q 0.65)	Sum	Producer acc.
Firn (in situ)	98894	413	99307	99.58%
Ice (in situ)	19426	21897	41323	52.99%
Sum	118320	22310	140630	
User acc.	83.58%	98.15%		Overall acc. 85.89%

361 **Table S1.** Contingency table summarizing the performance of the algorithm in correctly
362 retrieving porous firn and ice using quantile 0.65 of the ice content distribution as the
363 threshold differentiating between porous firn and ice compared to the in-situ ice content
364 being the reference. Values are in pixels. The producer's accuracy (producer acc.) relates
365 to omission errors, e.g. not retrieving ice when it is ice, while the users' accuracy (user
366 acc.) relates to commission errors, e.g. retrieving porous firn as ice. The overall accuracy
367 (overall acc.) relates to how well the algorithm performs in correctly retrieving both ice
368 and porous firn compared to the reference radargram.

369

	Firn (Q 0.79)	Ice (Q 0.79)	Sum	Producer acc.
Firn (in situ)	92999	6308	99307	93.65%
Ice (in situ)	11001	30322	41323	73.38%
Sum	104000	36630	140630	
User acc.	89.42%	82.78%		Overall acc. 87.69%

370 **Table S2.** As Table S1, using quantile 0.79 of the ice content distribution as the
371 threshold.

	Year	Well-developed		In development		In initiation	
		[Q _{0.25} ; Q _{0.5} ; Q _{0.75}]	Change	[Q _{0.25} ; Q _{0.5} ; Q _{0.75}]	Change	[Q _{0.25} ; Q _{0.5} ; Q _{0.75}]	Change
C	2010	[7.7; 10.5; 13.6]	+2%	[3.7; 4.6; 5.1]	+62%	-	-
	2017	[6.0; 10.0; 15.0]		[5.0; 6.5; 8.5]		[4.5; 5.5; 6.0]	
D	2010	[11.5; 13.3; 15.5]	+11%	[2.6; 3.5; 4.4]	+101%	-	-
	2018	[12.5; 15.0; 16.5]		[5.0; 6.5; 9.0]		[4.5; 5.5; 6.0]	
F	2010	[12.6; 15.0; 16.4]	-2%	[3.0; 4.2; 5.1]	+194%	-	-
	2017	[12.5; 14.0; 15.0]		[9.0; 11.5; 15.0]		[4.0; 5.0; 5.5]	

372 **Table S3.** Summary statistics table of ice content on three transects in Fig. 3 (transects C,
373 D, F), for the three stages of ice slab development at the start and end of the studied
374 period. Q_{0.25}, Q_{0.5}, Q_{0.75} correspond to quantiles 0.25, 0.5 and 0.75 of ice content
375 respectively. The ice content change represents the relative change of ice content by
376 2017 compare to 2010.